High Transverse Momentum 2-Jet and 3-Jet Cross Section Measurements in Photoproduction

Paul Bate

December 1999

THE UNIVERSITY
of MANCHESTER

High Energy Group
Department of Physics and Astronomy

A thesis submitted to The University of Manchester for the degree of
Doctor of Philosophy in the Faculty of Science and Engineering

---

Contents

Abstract

Using data from the H1 detector at HERA, *ep* cross sections in high transverse momentum, P_T^{jet} and high mass are presented for 2-jet and 3-jet event configurations. The data were taken between 1994 and 1997 and correspond to an integrated luminosity of 35.68 pb^{-1}. The kinematic regime was limited to $y < 0.9$ and $Q^2 < 4\mathrm{GeV}^2$ (photoproduction) by anti-tagging the electron in the Liquid Argon Calorimeter (LAC) and imposing a restriction on y_{JB} such that $y_{JB} < 0.9$.

In addition to testing the validity of QCD in the high P_T^{jet} photoproduction arena, the measurements are motivated by the excess of events with isolated leptons and missing P_T recently observed at H1. Similar kinematic configurations are studied but with only high P_T jets in the final state. Jets are defined using the Longitudinally Invariant K_T algorithm, with all selected events having one jet of $P_T^{jet1} > 25$ GeV and a second with $P_T^{jet2} > 15$ GeV. This asymmetric jet cut ensures the stability of the next-to-leading order QCD predictions for the 2-jet cross sections. For the 3-jet cross sections, a third jet of $P_T^{jet3} > 10$ GeV is required. All jets are required to lie in the pseudorapidity, η range $-0.5 < \eta^{jet} < 2.5$, in order that they be fully contained in the LAC.

The hadronic *ep* cross sections fall by three orders of magnitude in the measured ranges. The dominant error on the measurement arises from the uncertainty in the jet energy scale. In the highest mass and P_T^{jet} bins, statistical errors also become significant. When compared to QCD predictions from the event generators PYTHIA 5.7 and HERWIG 5.9, which include $\mathcal{O}(\alpha_s^2)$ matrix elements, parton showering and a hadronisation scheme, and a $\mathcal{O}(\alpha_s^3)$ numerical integration program (JetViP 1.1), no significant deviations are observed. The PYTHIA and HERWIG predictions both require an overall scale factor to be applied, while the normalisation of the JetViP result agrees well with the data. It is concluded that for the measurements made, no additional contributions from hadronic heavy particle decay are required.

No portion of the work referred to in this thesis has been submitted in support of an application for another degree or qualification of this or any other institute of learning.

The ownership of any intellectual property rights which may be described in this thesis is vested in the University of Manchester, subject to any prior agreement to the contrary, and may not be made available for use by third parties without the written permission of the University of Manchester, which will prescribe the terms and conditions of any such agreement.

Further information on the conditions under which disclosures and exploitation may take place is available from the Head of Department of Physics and Astronomy.

This work was supported financially by the Particle Physics and Astronomy Research Council (P.P.A.R.C.) between October 1996 and September 1999.

Chapter 1

Introduction

The structure of matter has been probed extensively in Deep Inelastic Scattering (DIS) lepton-proton collisions [1–4]. This led to the discovery of proton structure in the 1960's and the suggestion that all hadrons were composed of pointlike partons. Subsequently, the strongly interacting theory of quarks and gluons (QCD) was proposed and has enjoyed considerable success in predicting a range of measurements ever since.

The building of HERA, the first lepton-hadron collider, has allowed detailed proton structure measurements in previously unexplored kinematic regions [5, 6]. 27.6 GeV leptons collide with 820 GeV protons in a 6.3km ring. However the wealth of physics available for study at HERA stretches far beyond the traditional measurements of proton structure. The structure of real and virtual photons has been investigated, as have diffractive and Heavy Flavour physics. Several searches for evidence of physics beyond the Standard Model have also been performed. The study of collisions between protons and almost on-shell photons (photoproduction) has been of particular interest, with the photon-proton centre-of-mass energy being extended by an order of magnitude over previous fixed target experiments. Such high energies allow hard scattering processes to be clearly observed via their characteristic

hadronic jet structure.

In this thesis, the most energetic photoproduction collisions are analysed. Using the full luminosity achieved in HERA's positron-proton mode between 1994 and 1997, jet cross section measurements in invariant mass and transverse momentum, P_T^{jet} are extended to previously unmeasured values. A dual motivation for these measurements exists. Firstly, the cross sections may be compared to the predictions of QCD in order to test the validity of the theory in the high energy photoproduction environment. Secondly, recent measurements by the H1 collaboration have revealed an excess of events consistent with the production and subsequent leptonic decay of a heavy particle. In the past, similar analyses studying hadronic heavy particle decays have been blighted by poor understanding of the QCD 'background', a problem which can be avoided by using the measurements presented in this thesis.

In Chapter 2 the H1 detector is presented, concentrating on the components used to make the cross section measurements. Chapter 3 reviews the theoretical models of ep and γp interactions. The jet algorithms used in the analysis are defined and the computer programs that implement the physics processes are discussed in Chapter 4. Chapter 5 details the full analysis chain from event selection to the correction made for detector effects and the systematic errors considered. A discussion of the cross section measurements is presented in Chapter 6, along with a comparison to the QCD predictions modelled by the event generators PYTHIA 5.7 [7] and HERWIG 5.9 [8] and the numerical integration program, JetViP 1.1 [9]. The final chapter provides a summary of the measurements made and looks at future prospects for high P_T^{jet} analyses.

Chapter 2

The H1 Experiment at HERA

The H1 detector [10] is one of two colliding beam experiments found on HERA (the Hadron Electron Ring Accelerator). Since 1992, it has been used to study electron-proton and positron-proton scattering over a wide kinematic range. In this chapter the HERA accelerator will be presented, followed by a overview of the H1 detector and a more detailed look at the detector components relevant to the measurements described in Chapter 5.

2.1 The HERA *ep* Collider

Situated in Hamburg, HERA is chiefly composed of two approximately circular, 6.3km circumference beam-pipes. In one, electrons[1] are accelerated up to 27.6 GeV while in the other, protons are injected and ramped[2] to 820 GeV . Two beam-pipes are required since the differing mass and energies of the beam particles requires

---

[1] The machine group at HERA is capable of switching from electrons to positrons and back and has done so in line with experimental need on several occasions. In the period relevant to this thesis, positrons were used. However, the beam lepton will be referred to as an electron, regardless of its charge.

[2] since 1998, the proton beam energy has been increased to 920 GeV .

separate magnetic configurations. Furthermore, a greater flexibility in altering individual beam energies is possible with separate beam pipes. Superconducting and non-superconducting magnets are used to accelerate the beams and bring them together (within a single beam pipe) at two interaction points; in the South Area, where the ZEUS detector is situated and in the North Area, where H1 is found. Two further fixed target experiments are located on the HERA ring. On the East side, a portion of the electron beam can be steered into a range of polarised gaseous targets, for analysis with the HERMES detector. On the opposite side of the ring, the HERA-B experiment uses the proton beam to study B-physics via interactions with a set of up to eight target wires.

Each beam is concentrated into small pulses or bunches. A subdivision into colliding and non-colliding (pilot) bunches is made. In colliding bunches, a proton bunch is paired with an electron bunch, resulting in a crossing every 96 nanoseconds. The pilot bunches have no corresponding bunch in the opposite beam and so can be used to estimate the rate of interactions between a beam and the residual gas in the beampipe (beam-gas interactions) and between the beam and the beampipe itself (beam-wall interactions). In the period 1994-1997, there were typically 160 colliding bunches and 10 pilot bunches per luminosity fill.

2.2 An overview of the H1 Detector

The H1 detector, a schematic of which is shown in figure 2.1, is a system of multiple subdetectors and components used for tagging and identifying the properties of elementary particles produced in lepton-hadron collisions. It offers almost full 4π solid angle coverage. The main region not covered is that occupied by the beam pipe.

Figure 2.1 also shows the reference frame used by H1. A right-handed set of

Cartesian coordinates (x, y, z) is used, with the incoming proton beam defining the positive z direction. The spherical coordinate set (r, θ, ϕ) is then defined with reference to the Cartesian coordinates in the standard way, such that $\theta = 180°$ corresponds to the direction of the incoming electron.

Particle identification is achieved in two ways - by tracking and calorimetry. A set of tracking detectors surrounding the nominal interaction point record the path taken by charged particles passing through them. A 1.15T magnetic field curves the paths of these particles, from which their momentum may be measured. Beyond the trackers lie calorimeters, which absorb almost all the energy of the incident particles. The energy is converted into a measurable signal which, due to the finely segmented nature of the calorimeters, allows an energy deposition profile to be built up and so particle detection to be achieved. For example, an electron tends to produce a much more collimated energy deposition than a hadron.

The complementary nature of tracking and calorimetry is illustrated by the following examples.

- While the tracking system uses track curvature to clarify a particle's charge, neutral particles (which will pass undetected through the trackers) are recorded in the calorimeters.
- Low momentum particles may not reach the calorimeters but their small radius of curvature allows their momentum to be accurately measured using the trackers. Even for those low momentum particles that do enter the calorimeters, the calorimeter energy measurement will be poor due to the $1/\sqrt{E}$ term inherent in the resolution of sampling calorimeters.
- High momentum tracks have little curvature and the errors on the track momentum become high. However, the energy of such particles will be well measured by the calorimeters.

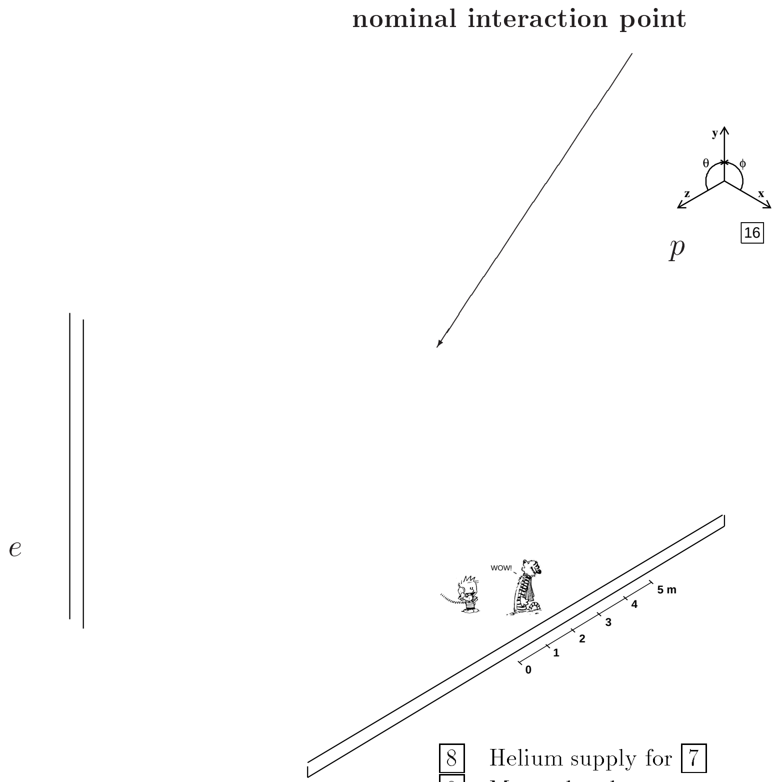

1	Beam pipe and beam magnets	8	Helium supply for 7
2	Central track detectors	9	Muon chambers
3	Forward track detectors	10	Instrumented iron yoke
4	Electromagnetic LAr calorimeter	11	Forward muon toroid
5	Hadronic LAr calorimeter	12	SPACAL and Backward DC
6	Superconducting coil (1.15 T)	13	PLUG calorimeter
7	Compensating magnet	14	Concrete shielding
		15	Liquid argon cryostat
		16	H1 coordinate system

Figure 2.1: *The H1 Detector.*

In order to separate and accurately measure genuine *ep* physics events from the large background caused by cosmic rays, beam-gas and beam-wall interactions, stringent demands are made on the H1 detector.

- Sophisticated triggering is required in order to isolate *ep* events. A multi-level triggering system is used to cope with the short time intervals between colliding bunches, with decisions being made as early as possible to reduce the dead-time during luminosity fills.
- Although both beams are ultra-relativistic (so that rest masses become negligible when calculating the centre-of-mass collision energy), the large difference in beam energies means that the centre-of-mass of the *ep* system is thrown forward in the laboratory frame. This necessitates a very asymmetric detector.
- A wide range of final states must be measured in the detector. The presence or absence of the scattered electron is essential in determining the kinematics of the interaction. In addition, the transverse momentum balance must be well measured to isolate charged current events. The tracker and calorimeter outputs are combined to achieve the high spatial and energy resolution and electron detection efficiency required.
- Exotic phenomena, as well as standard Heavy Flavour decays, can be signalled by the presence of muons in the final state. Muon identification is therefore also essential and is provided by the Central and Forward Muon Detectors.

As mentioned above, the H1 detector is highly asymmetric. In the forward (positive z) direction, emphasis is placed on detecting the high energy hadronic jets using finely segmented calorimeters. Kinematically, the scattered electron is most likely to be found in the backward (negative z) region and so purpose built trackers and calorimeters are found here to maximise electron detection efficiency. Below, a discussion of the main detector components is presented.

2.3 Calorimetry

At H1, there are four distinct calorimeters. The Liquid Argon Calorimeter (LAC) [11] (figure 2.2), is the main calorimeter used for the detection of the hadronic final state (HFS) and the electron identification for high Q^2 events. It is a sampling calorimeter with full azimuthal coverage and extends in polar angle over the range $4^\circ < \theta < 154^\circ$, corresponding to a pseudorapidity[3], η range of $-1.46 < \eta < 3.35$. The SpaCal [12], a spaghetti calorimeter, is found in the backward region and is mainly used for electron identification, although its hadronic section also allows backward jets to be identified. Both these calorimeters are used in this thesis. The Instrumented Iron and the Plug, the remaining H1 calorimeters, have specialised uses and are not included in the analysis. The LAC will be used as a case study of how calorimeters work.

2.3.1 The Liquid Argon Calorimeter

Sampling calorimeters consist of two main materials - passive layers that cause particles to lose energy, interleaved with active layers that sample the resulting energy deposition. The LAC consists of an electromagnetic (EMC) section, where 2.4mm thick plates of lead are used as absorbing material, and a hadronic (HAC) section which uses 16mm stainless steel plates as absorbers. The larger size of the stainless steel over the lead plates reflects the greater time taken for hadronic showers to develop in a medium. Both sections use Liquid Argon as the active material. The LAC has a ‘wheel’ structure. Eight wheels, from the furthest forward IF1 to the most backward BBE (the only wheel to lack a hadronic section) exist and each has been individually calibrated to better understand and improve the LAC resolution [13].

---

[3] $\eta = -ln[tan(\frac{\theta}{2})]$

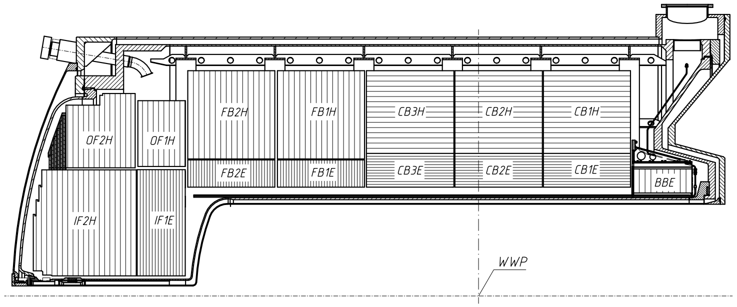

Figure 2.2: *A side view of part of the Liquid Argon Calorimeter, showing the wheel structure. WWP denotes the nominal interaction point.*

Electromagnetic and hadronic particles deposit their energy via different mechanisms. When an energetic electromagnetic particle passes through a thick absorber, bremsstrahlung and pair production processes occur and the particle rapidly loses energy. The secondary particles undergo similar interactions and a shower is built up. As the particles within the shower lose energy, ionisation becomes increasingly important as a source of energy loss. The radiation length, $X_\circ$, defined as the mean distance taken for an electron travelling through a medium to lose all but $\frac{1}{e}$ of its energy, is used to characterise the absorbing quality of the medium for electromagnetic particles. Lead has a radiation length of 0.56cm.

For hadronic particles, both elastic and inelastic scattering with nucleons in the absorber occur. Secondary hadrons are produced and again a shower develops. The interaction length, λ_I is used to characterise the longitudinal development of a hadronic shower (lead and steel both have $\lambda_I \approx 17$cm). Hadronic shower development ends when the hadrons have sufficiently low energy to be stopped by ionisation or nuclear capture. Typically, the lateral and longitudinal extent of a hadronic

shower is greater than that of an electromagnetic shower. This observation is the basis for discriminating between particle types using calorimetry.

As the shower passes through the absorber, it is periodically sampled by layers of active material. At H1, the Argon atoms are ionised by the shower particles and the resulting charge is read out using rectangular cathode pads a few centimetres in size. Argon is chosen for its high atomic density (which leads to large ionisation) and because Argon's closed electron shell structure prevents the ions and electrons undergoing further inelastic scatters. The HAC is deeper ($\sim 7\lambda_I$) in the forward region, where many highly energetic particles are expected (due to the asymmetry of the beam energies), reducing to $\sim 5\lambda_I$ in the backward region. Similarly, the EMC varies from $\sim 30X_\circ$ to $\sim 20X_\circ$.

The LAC is an example of a non-compensating calorimeter. This means that the response to electromagnetic and hadronic particles is not equal; hadrons on average result in $\approx 30\%$ less energy deposition than electromagnetic particles of the same original energy. This reflects the energy lost by hadrons to nuclear excitation or breakup in the absorber.

The highly segmented nature of the LAC is reflected in the ∼45000 readout channels it contains. Both EMC and HAC readout channels are combined into a total of 256 towers, built up such that they point towards the nominal interaction point. This pointing technique allows the transverse energy (the energy projection perpendicular to the z axis) as well as the energy to be summed for each tower and this information is used as the basis of the LAC triggering system. The exceptional granularity of the LAC allows e/π discrimination at a level of 10^{-3} once isolated cells, consistent with electronic noise, have been removed offline. In test beam studies, the energy resolution[4] has been shown to be consistent with $\frac{\sigma_E}{E} \approx \frac{0.12}{\sqrt{E}} \oplus 0.01$ for electrons and $\frac{\sigma_E}{E} \approx \frac{0.50}{\sqrt{E}} \oplus 0.02$ for charged pions. The above resolutions have been verified by tests undertaken after installation of the H1 detector on the HERA ring.

---

[4] Unless otherwise stated, all energies are given in units of GeV.

The overall electromagnetic energy scale is currently known to 1.5% [14], obtained by comparing the measured track momentum of positrons and electrons with their LAC energy deposition. By studying the transverse momentum balance in DIS events, the hadronic energy scale is then inferred to an accuracy of 4% [14].

2.3.2 The SpaCal

Like the LAC, the SpaCal (figure 2.3) is a non-compensating sampling calorimeter split into hadronic and electromagnetic sections. It is situated in the backward region, spanning the angular range $-1.43 < \eta < -3.82$ and so filling the gap between the most backward part of the LAC and the beampipe. Both sections are made up of scintillating fibres (the active component) embedded in an (absorbing) lead matrix. The active volume of the electromagnetic section is 25cm deep with a lead-to-fibre ratio of 2.3:1, corresponding to 28 radiation lengths. The hadronic section is one interaction length deep and has a lead-to-fibre ratio of 3.4:1. Scintillation light is detected using photomultiplier tubes and read out into 1328 channels. Test beam results are consistent with an energy resolution $\frac{\sigma_E}{E} \approx \frac{0.7}{\sqrt{E}} \oplus 0.01$ in the electromagnetic section and a hadronic energy resolution of $\frac{\sigma_E}{E} \approx \frac{0.56}{\sqrt{E}} \oplus 0.03$. The overall energy scale of the hadronic and electromagnetic sections is known to within 7%.

It should be noted that the SpaCal was introduced in 1995, when it replaced the BEMC (a purely electromagnetic calorimeter). This thesis uses data taken in the period 1994-1997 and approximately 7% of the integrated luminosity was taken while the BEMC was in place. The overall electromagnetic energy scale of the SpaCal and BEMC are similar and throughout the analysis, the assumption has been made that the SpaCal was in place. This leads to a small inaccuracy which is factored into the systematic error analysis and is negligible in comparison with the uncertainty arising from the overall energy scale of LAC.

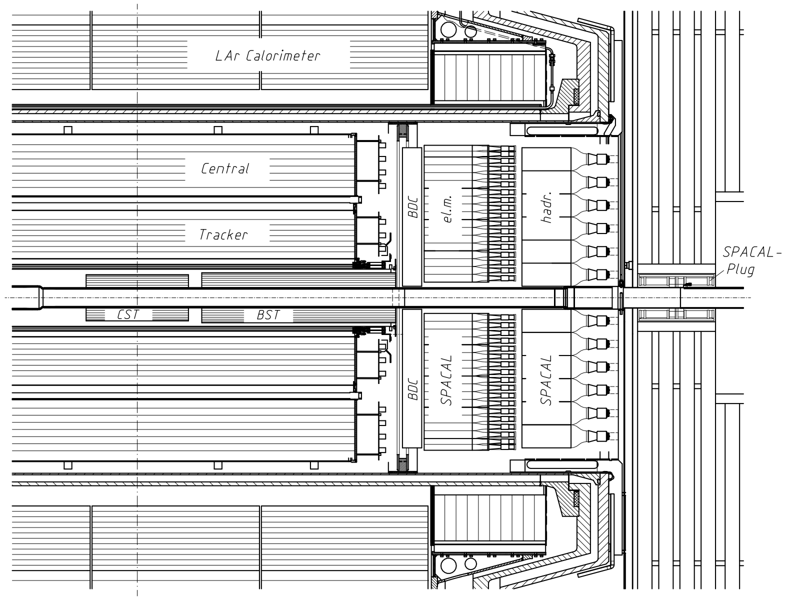

Figure 2.3: *Partial side view of the H1 detector including the SpaCal and part of the Central Tracker and LAC.*

2.4 Tracking

H1 includes several tracking detectors (figure 2.4), centred about the nominal interaction point and embedded in the 1.15T magnetic field parallel to the z axis. The field is provided by a superconducting solenoid encasing the calorimeters. Two types of tracker are used: Drift Chambers and Multiwire Proportional Chambers (MWPC's).

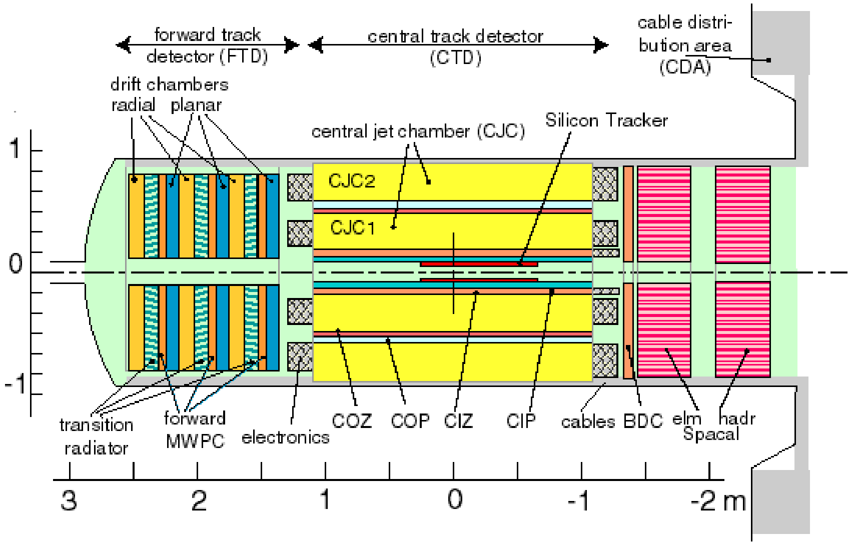

Figure 2.4: *An $r - z$ View of the Tracking Detectors at H1*

2.4.1 Drift Chambers

A drift chamber is made up of many cells, each cell consisting of a set of anode (sense) wires surrounded by cathode wires or pads. The whole cell is gas-filled and field-shaping wires, separating the sense wires, ensure that a uniform electric field, **E** exists across the cell. A charged particle passing through the cell will ionise the gas and the released electrons drift with near uniform velocity towards the sense wires (whilst the ions move toward the cathode). Close to each sense wire, the **E** field increases dramatically and further ionisation occurs, resulting in an avalanche of electrons and ions. As these ions move towards the cathode, a significant current is induced on the sense wire. This signal is then amplified before being digitized by an FADC (flash analogue to digital converter). This is known as a hit. Since the position of the sense wire is known to a typical precision of 50μm and the drift velocity is a known function of the **E** field, the drift time can be associated with a distance of closest approach of the trajectory of the original charged particle to the sense wire. By reading the signal out at both ends of the sense wire and comparing the charge deposited, the coordinate of the hit along the sense wire can be obtained. Hits in several cells are built up and the particle trajectory is reconstructed as a track.

2.4.2 MWPC's

In an MWPC anode (sense) wires are strung across a gas-filled chamber with cathode wires or pads placed around the outside. As with drift chambers, the passage of a charged particle causes ionisation and the electric potential causes electrons and ions to move towards the anode and cathode respectively. The close spacing of the sense wires ensures that rapid amplification of the initial ionisation occurs and a significant signal is observed from the induced current in the sense wires. Since the amplification regions around the sense wires overlap in an MWPC, spatial resolution is limited to the distance between sense wires. This limits the resolution to a few mm but results in very accurate timing of the hits, which drift chambers lack due to the longer drift times. Therfore drift chambers and MWPC's complement each other and together give accurate information which can be used for event reconstruction amd triggering.

2.4.3 The H1 Trackers

The H1 tracking system is split into three main sections. The Forward Track Detector [15] consists of three identical supermodules, each containing a planar and radial drift chamber, a passive transition radiator and a multiwire proportional chamber. The polar angle range covered is $7° < \theta < 25°$. In the backward region lies the Backward Drift Chamber and Backward Multiwire Proportional Chamber. Between the Forward and Backward tracking systems lies the Central Track Detector (CTD). Only the CTD is used in this thesis.

The main components of the CTD are the two cylindrical drift chambers, CJC1 and CJC2 [16], situated concentrically about the beam axis (figure 2.4). The setup of the two chambers is essentially identical, both having the plane of the sense wires parallel to the z axis. By inclining each cell (see figure 2.5) at 30° with respect to the radial direction, stiff tracks are made to pass through several drift cells, greatly improving the track reconstruction. A high resolution in the $r - \phi$ plane of $\sigma_{r-\phi} \approx 350\mu$m is achieved by drift time measurements while charge division techniques limit the z resolution to $\sigma_z \approx$ 5cm.

Since the z resolution is considerably poorer in CJC1 and CJC2 than that in the $r - \phi$ plane, two extra detectors, the Central Inner Z Chamber (CIZ) and Central Outer Z Chamber (COZ) [17], have been specifically designed to reduce σ_z. CIZ is positioned inside CJC1 while COZ lies between CJC1 and CJC2. Both are drift chambers with the sense wires strung azimuthally and the $\mathbf{E}$ field in the z direction, so that the z coordinate may be determined from drift time measurements with a precision of $\sigma_z \sim$ 200-500 μm.

Complementing the accurate spatial resolution of the H1 drift chambers are two MWPC's, the Central Inner Proportional (CIP) and Central Outer Proportional (COP) Chambers [18]. These are again concentric with the beampipe and lie next to CIZ and COZ respectively. Their swift time response makes them the main detectors used in the H1 z-vertex trigger.

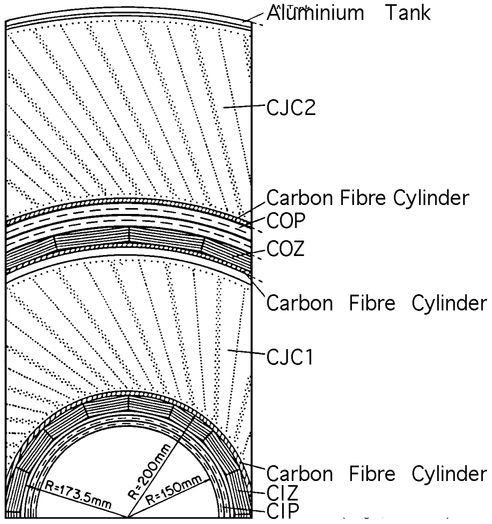

Figure 2.5: *An $r - \phi$ view of the Tracking Detectors at H1.*

2.5 The Scintillation System

At HERA, the rate of genuine *ep* events is considerably lower than that of proton induced beam-gas and beam-wall interactions. To reduce this background, scintillators are placed upstream (from the proton viewpoint) of the nominal interaction point. Beam-gas and beam-wall events will cause scintillation at approximately the same time as the proton bunch passes through the scintillators. In contrast *ep* events, being centred around the nominal interaction point, will result in particles arriving $\sim \frac{2\Delta z}{c}$ later, where Δz is the distance in z between the nominal interaction point and the scintillator. This corresponds to a time difference of ≈13ns for the Time of Flight (ToF) System [19] situated at z=-2m while for the Veto walls situated at z=-6.5m and z=-8.1m, the time difference is ≈22ns and ≈27ns respectively.

Since the ToF system has a resolution ≈4ns and the inner and outer Veto Walls have resolutions of ≈3ns and ≈8ns respectively, all may be used to trigger ep events and reject non ep interactions.

2.6 The Luminosity System

The Luminosity System (figure 2.6) consists of a photon tagger at z=-103m and an electron tagger at z=-33m. Both are crystal calorimeters, the photon detector being a 5x5 array and the electron tagger a 7x7 array. The luminosity is calculated by measuring the number of events arising from a process with a precisely calculated cross section: the Bethe-Heitler process [20]; $ep \rightarrow ep\gamma$. Events are registered when hits in the electron and photon taggers are observed in coincidence. Accurate parameterisation of the electron tagger acceptance is required since the acceptance is below 50% (the photon detector has an acceptance of ≈ 98%). This is achieved using a tuned Monte Carlo simulation.

Two further electron taggers exist at z=-8m and z=-44m, with the result that almost the entire y range is covered. None of the electron taggers is used in this thesis, other than the 33m tagger for the luminosity measurement.

2.7 Data Acquisition and Triggering

With a bunch crossing every 96ns, H1 is presented with a readout problem since many subdetectors take considerably longer than this to register information. For example, drift times up to 1μs are possible in the drift chambers. It takes ∼24 bunch crossings before all information from the ∼270 000 readout channels for a single bunch crossing is passed from the subdetectors, in the form of 8-bit trigger elements, to the central trigger [21]. The solution used is to 'pipeline' the readouts i.e. to buffer the information until the central trigger has made a decision to keep an event.

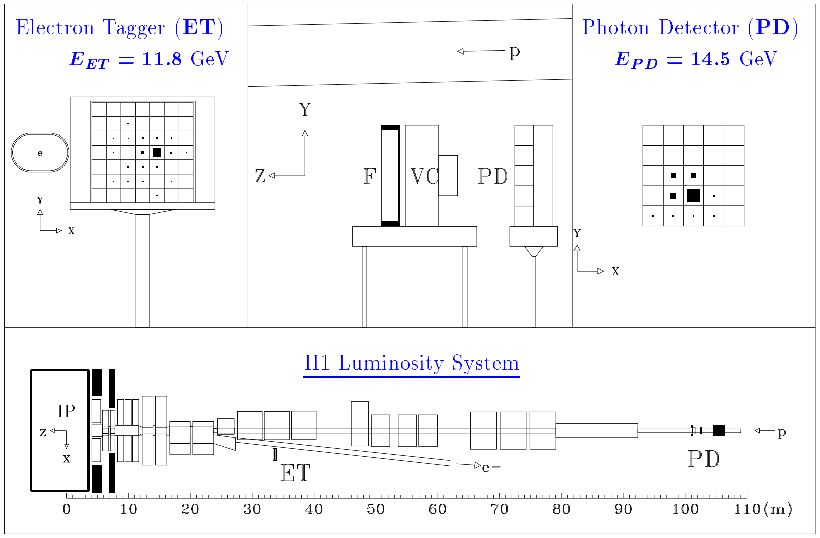

Figure 2.6: *Schematics of the H1 Luminosity System. Clockwise from top left, a hit in the 33m electron tagger (the electron beampipe is represented by the oval to the left of the tagger); the photon detector position relative to the proton beampipe; a hit in the photon detector; the H1 Luminosity System, relative to the main H1 detector.*

The H1 triggering system (figure 2.7) has several levels, varying in complexity and consequently speed. Level 1 (L1) is the coarsest and fastest trigger level and so is the first stage of the triggering system. The Central Trigger takes information from ∼ 200 trigger elements and combines them into a ∼ 140 subtriggers, based on expected physics signals, using lookup tables with variable thresholds. For example, subtrigger 64 (used extensively in this thesis) requires significant energy deposition in the LAC along with a good timing requirement from either the LAC or MWPC's and no signal consistent with a background event in the Scintillation System. If any subtrigger is 'verified' (has all its trigger bits set), L1 accepts the event[5]. A signal is then sent to each subdetector, pipelining ceases and the full event information is passed to the Central Event Builder (CEB). During this time, no information is recorded and so deadtime results. Typically, ≈ 10% deadtime is observed, which is the price paid for reducing the background rate of more than 10kHz to an event rate of a few tens of Hz, without significant loss of *ep* events for the majority of physics channels.

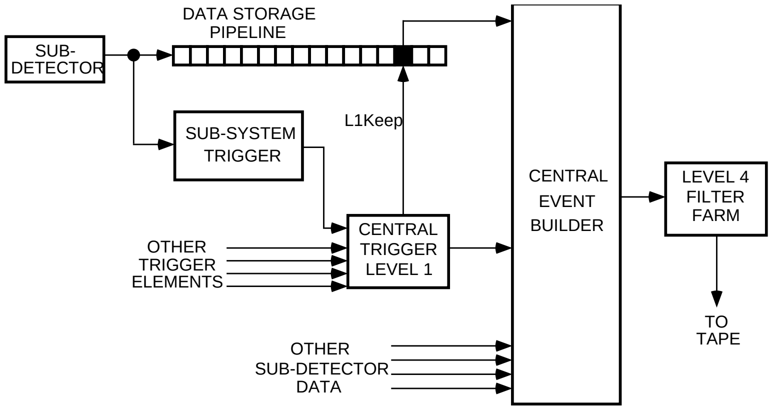

Figure 2.7: *A schematic of the H1 data acquistion and triggering system. L2 is not shown.*

The next step of the H1 trigger is Level 2 (L2). This is a parallel system of neural networks and topological triggers and like L1 works online. However, it is more

---

[5] To avoid being overwhelmed by high rates, some frequently firing subtriggers are prescaled. Each time the subtrigger fires, a counter is incremented. A prescale of n implies that when the counter reaches n, the subtrigger is verified and the counter reset, otherwise the subtrigger is assumed not to have fired for purposes of accepting the event.

sophisticated and hence slower than L1, delivering a decision in $\approx 20\mu s$. L2 is a recent addition to the triggering system (1995) and is only implemented for certain channels. The subtriggers used in this thesis all bypass L2. For historical reasons, the next layer of the trigger system is Level 4.

L4 is a PC farm which effects a fairly detailed reconstruction of the entire event. It is the last stage at which the H1 Trigger System may throw away events. A set of cuts is applied, depending on the subtrigger that fired at L1 and occasionally the L2 information. Approximately 5-10 events pass L4 each second, with almost all of the background events from beam-gas, beam-wall, cosmics and trigger noise being rejected. These events are then passed to an SGI machine for Level 5 processing offline, using the full reconstruction code. L5 classifies each event into one or more physics classes, each class being definined by a set of physics-inspired cuts. All events are written to disk at this stage.

It should be made clear at this point that the generic term 'subtrigger' can be used to mean several things. In particular, there are L1 subtriggers and L4 subtriggers. While an L1 subtrigger only uses information from L1 trigger elements, L4 subtriggers may have additional requirements imposed at L2 and/or L4. Unless specified, 'subtrigger' will be taken to mean L4 subtrigger from here on.

2.8 Monte Carlo Simulation

In order to correct for the effects of detector smearing and finite acceptance, H1 uses the GEANT3 [22] code to provide a full simulation of the detector. Events generated by the Monte Carlo programs listed in section 4.6 are subjected to this simulation and the output from each subdetector is reconstructed in an identical fashion to the data. A comparison can then be made between the data and the simulated and reconstructed Monte Carlo events. The contribution from different physics processes (e.g. photoproduction, DIS) can be assessed, the accuracy of the detector modelling tested, background processes subtracted on a statistical basis and (by comparing the Monte Carlo distributions before and after detector simulation and reconstruction), a correction for detector effects made. This procedure will be illustrated in more detail in Chapter 5.

Chapter 3

Physics at HERA

This chapter gives an overview of the HERA physics relevant to the measurements presented in chapter 6. The kinematics of the HERA environment are considered and the structure of the proton and photon reviewed. After establishing the similarities and differences between Deep Inelastic Scattering and photoproduction, the latter is examined in more detail, leading on to the explanation of high P_T^{jet} production, given in chapter 4.

3.1 HERA Kinematics

In the generic neutral current (NC) DIS interaction at HERA, $ep \rightarrow eX$ (figure 3.1), the final state consists of the scattered lepton and a hadronic system, X formed by the scattered parton[1] and the proton remnant. For fixed beam energies, two variables are required to constrain the kinematics of the DIS process. However, it is convenient to define several variables and then use those most appropriate for a particular problem. The main variables used in DIS are given below.

---

[1] Partons are the pointlike constituents of the proton.

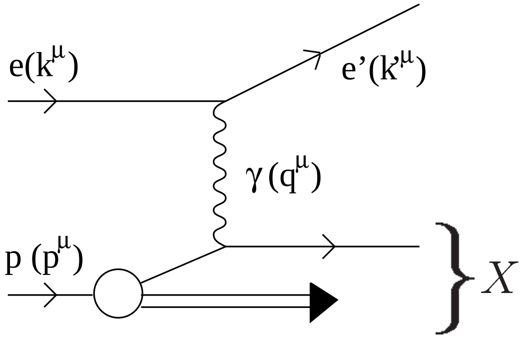

Figure 3.1: *A neutral current DIS scattering process showing the HERA kinematics.*

The negative square of the 4-momentum transferred between the incoming particles is denoted Q^2 , so that

$$Q^2 = -q^2 = -\left(k - k^{'}\right)^2 \tag{3.1}$$

while s, the squared centre-of-mass energy[2], is given by

$$s = (k + p)^2. \tag{3.2}$$

Two scaling variables are commonly used in HERA physics. The first, Bjorken-x is defined as

$$x = \frac{Q^2}{2p.q}. \tag{3.3}$$

In the infinite momentum frame of the proton (or equivalently, when the struck parton is collinear to the proton), x represents the fraction of the proton's 4-momentum carried by the struck parton. The other scaling variable, y is given by

$$y = \frac{p.q}{p.k} \tag{3.4}$$

---

[2] Between 1994 and 1997, when HERA collided 820 GeV protons with 27.6 GeV electrons, s=90600 GeV^2 .

and may be interpreted (in the proton rest frame) as the fraction of the electron's energy carried by the photon. Both x and y take values between zero and unity. The invariant mass of the γp system, W, defined in equation 3.5

$$W^2 = (q + p)^2 \tag{3.5}$$

is also often used in HERA physics. The quantities above may be related (neglecting incoming particle masses) by

$$Q^2 = sxy \tag{3.6}$$

$$W^2 = Q^2 \left(\frac{1 - x}{x}\right). \tag{3.7}$$

A photon exchange process is used in figure 3.1 to demonstrate the HERA kinematics. Neutral current Z boson exchange and charged current (CC) W boson exchange are also observed at HERA [23,24] however at low Q^2 the high mass of these bosons greatly suppresses such interactions with respect to photon exchange.

3.2 Deep Inelastic Scattering

The structure of the proton can be investigated via DIS, in which the highly virtual photon resolves the partons inside the proton. The structure functions of the proton, $F_1(x, Q^2)$ and $F_2(x, Q^2)$, and the parity-violating $xF_3(x, Q^2)$ are built up from parton distribution functions ($PDF's$), denoted $f_i(x, Q^2)$. $f_i(x, Q^2)\ dx$ gives the number of partons of type i with momentum fraction between x and $x + dx$ when the proton is probed at a scale Q^2. An intuitive feel for structure functions can be obtained by considering the Quark Parton Model (QPM), in which quarks are the only constituents of the proton, and interact only electromagnetically. The virtual photon strikes a single parton with fractional momentum x, scattering it out of the proton. In the QPM, $F_1(x, Q^2)$ and $F_2(x, Q^2)$ are given by

$$2xF_1(x, Q^2) \ = F_2(x, Q^2) \tag{3.8}$$

and

$$F_2(x,Q^2) \;= \sum_i x e_i^2 f_i(x,Q^2)\ . \tag{3.9}$$

where the index i runs over all quarks and antiquark flavours and e_i is the charge of the i^{th} quark or antiquark.

When photon exchange dominates, the DIS cross section can be expressed in terms of $F_1(x,Q^2)$ and $F_2(x,Q^2)$ as

$$\frac{\mathrm{d}^2\sigma_{ep\to eX}}{\mathrm{d}x\mathrm{d}Q^2} = \frac{4\pi\alpha_{em}^2}{xQ^4}\left[xy^2F_1(x,Q^2) + (1-y)F_2(x,Q^2)\right]. \tag{3.10}$$

It can be shown that $F_1(x,Q^2)$ and $F_2(x,Q^2)$ are related to the cross sections for the scattering of longitudinally and transversely polarised photons, σ_L and σ_T by

$$\sigma_L = \frac{4\pi^2\alpha_{em}}{Q^2}(F_2 - 2xF_1) \tag{3.11}$$

$$\sigma_T = \frac{4\pi^2\alpha_{em}}{Q^2}2xF_1 \tag{3.12}$$

and this allows the DIS cross section to be written only in terms of F_2 and the photo-absorption ratio, $R = \frac{\sigma_L}{\sigma_T}$:

$$\frac{d^2\sigma_{ep\to eX}}{dxdQ^2} = \frac{4\pi\alpha_{em}^2}{xQ^4}\left[1 - y + \frac{y^2}{2(1+R)}\right]F_2(x,Q^2)\ . \tag{3.13}$$

It is interesting to note that since massless photons ($Q^2 = 0$ GeV^2) have no longitudinal component, equation 3.13 becomes independent of F_1.

The QPM gives rise to *scaling*, in which the structure functions depend only on x and not on the scale, Q^2 at which the proton is probed. However, detailed measurements by BCDMS [3], H1 [25] and ZEUS [26] have shown that while scaling is observed over several decades in Q^2 at relatively high x, a clear Q^2 dependence is seen (see figure 3.2) at lower x values.

A more sophisticated model of partonic structure is given by Quantum Chromodynamics (QCD), a non-Abelian gauge theory, invariant under $SU(3)$ colour

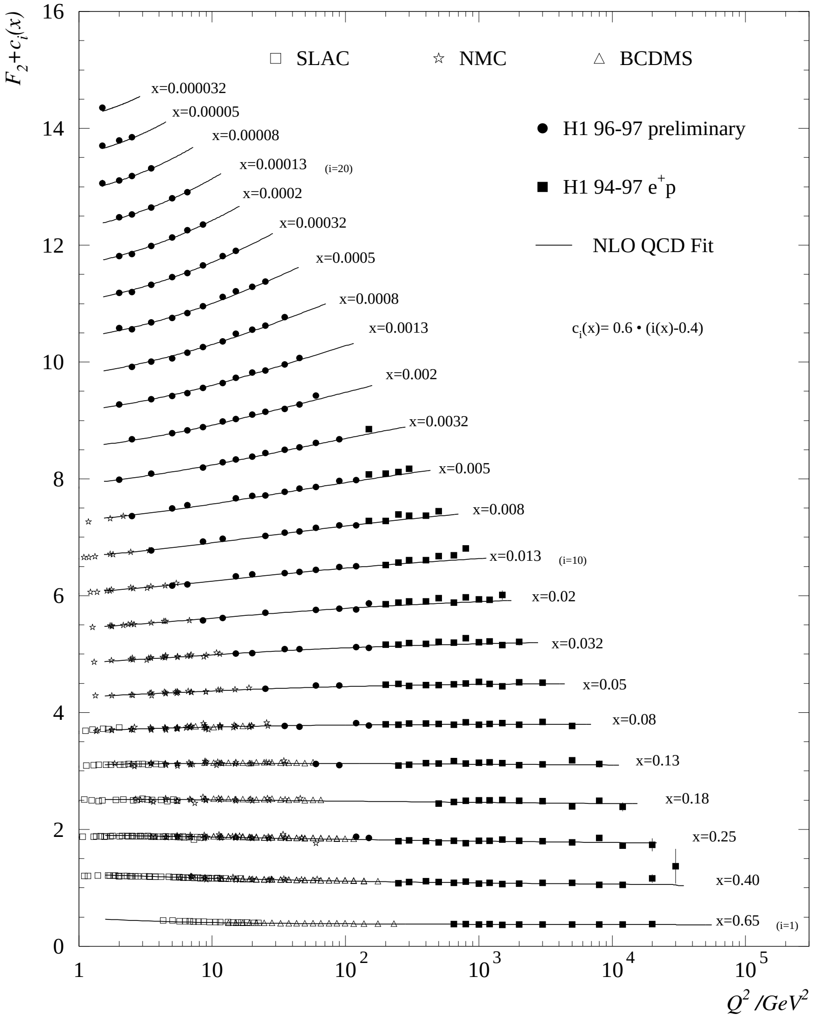

Figure 3.2: *$F_2(x,Q^2)$ as measured at HERA, and in fixed target experiments, as a function of Q^2. The curves are a phenomenological fit performed by H1 [14]. $c(x)$ is an arbitrary vertical displacement added to each point for visual clarity, where $c(x) = 0.6(i(x) - 0.4)$ and i is the x bin number such that $i = 1$ for $x = 0.65$.*

transformations. The gauge bosons are known as gluons and couple to the colour charge carried by all partons. Although QCD does not give absolute predictions for $PDF's$, the Q^2 evolution of the structure functions can be calculated in the HERA kinematic range, using the DGLAP evolution equations. These are integro-differential equations which take as input the $PDF's$ of gluons and quarks at a starting scale and predict the form of the $PDF's$ and so structure functions at a new scale. The DGLAP equations have been applied to low energy fixed target data to evolve the proton structure functions up to the Q^2 scales observed in the HERA environment. They agree well with the logarithmic rise of F_2 with Q^2 at low x seen in the data. This rise results from gluon emission from quarks and is related to the gluon density, $G(x, Q^2)$ by

$$G(x,Q^2) \sim \frac{\partial F_2(x,Q^2)}{\partial lnQ^2} \tag{3.14}$$

$PDF's$ are particularly useful since they are independent of the hard scatter that takes place between two partons. They are therefore universal - the structure function of a hadron may be measured in one environment (for example ep collisions at HERA) and then applied to a totally different arena, e.g. in hadron-hadron collisions at the Tevatron or LHC. The cross sections measured in this thesis use $PDF's$ extracted from combined fits to the data of many experiments.

3.3 ep and γp Physics

The variable Q^2 has an extremely useful physical interpretation. Although the proton does not have a clear radius, its size can be estimated from nuclear scattering experiments to be of order 10^{-15}m or $\sim$ 1 GeV in natural units. Using the Uncertainty Principle, Q^2 may be interpreted as the size scale for the interaction. Above $Q^2 \sim 1$ GeV^2 , the virtual photon will be able to probe the structure of the proton.

This is the classic DIS picture. Conversely, if Q^2 is well below the critical value, then the photon will be incapable of resolving the proton. This is the photoproduction or γp scenario. Since the photon propagator gives rise to a $1/Q^4$ factor in the total ep cross section, photoproduction dominates the HERA event rate. Although the transition from γp to DIS must be smooth, in the limits of high and low Q^2 , very different physics is seen. A wealth of interesting measurements can be made in both regimes. This thesis concerns measurements made using γp events.

3.4 Photoproduction Physics

In the γp picture, the electron can be viewed as a source of almost on-shell photons, with the interaction taking place between the photon and the proton. As noted in Section 3.2, for $Q^2 \ll 1$ GeV^2 , $\sigma_L \rightarrow 0$ and so $\sigma_T \rightarrow \sigma_{tot}^{\gamma p}$, the total photoproduction cross section. In this limit, the ep and γp cross sections are related by

$$\frac{d\sigma_{ep}}{dy} = f_{\gamma/e}(y)\ .\ \sigma_{tot}^{\gamma p} = \frac{\alpha_{em}}{2\pi}\left[\frac{1+(1+y)^2}{y} ln\frac{Q^2_{min}}{Q^2_{max}} - \frac{2(1-y)}{y}(1-\frac{Q^2_{min}}{Q^2_{max}})\right]\sigma_{tot}^{\gamma p}. \tag{3.15}$$

where $Q^2_{min} = \frac{m_e^2 y^2}{(1-y)}$ is the kinematic lower limit on Q^2 , m_e is the electron mass, Q^2_{max} is the upper Q^2 limit set by experimental conditions and $f_{\gamma/e}(y)dy$ gives the number of photons radiated in the fractional energy range y to $y + dy$ with virtuality between Q^2_{min} and Q^2_{max} . The results of H1 [27], ZEUS [28] and a variety of low energy experiments [29] for the total photoproduction cross section are shown in figure 3.3. The solid line is the prediction of the Donnachie-Landshoff (DL) [30] combined fit of hadron-hadron and low energy photoproduction data and the dashed line is the ALLM [31] parameterisation. The dotted line represents the DL parameterisation obtained after the measurement of the total $p\bar{p}$ cross section by the CDF collaboration [32] had been included.

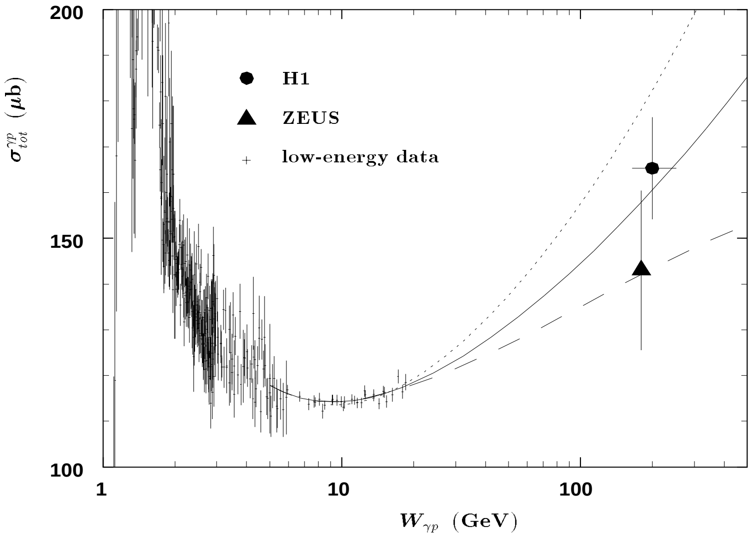

Figure 3.3: *The total photoproduction cross section,* $\sigma_{tot}^{\gamma p}$ *as a function of the* γp *centre of mass energy,* $W_{\gamma p}$ *measured using data from ZEUS, H1 and low energy experiments. The curves are fits made by Donnachie and Landshoff (solid and dotted lines) and the ALLM group (dashed line) to data sets which did not include the H1 and ZEUS points.*

3.5 Photon-Proton Interactions

Having factorised the ep cross section (equation 3.15), the interactions between photons and protons can now be considered. These are dominantly 'soft', peripheral interactions, characterised by low P_T ($\simeq 1-2$ GeV) final state particles. The lack of a hard scale in such processes prevents a reliable perturbative calculation. However, hard photon-proton interactions have been observed at HERA and are well described by QCD-inspired models.

3.5.1 Low P_T Interactions

Low energy fixed target experiments have shown that the photon does not interact solely as a gauge boson. Instead, interactions similar to those seen when two hadrons collide are observed. To explain this phenomenon, the Vector Meson Dominance (VMD) model was proposed, in which the photon fluctuates into a vector meson, V with the same quantum numbers (predominantly a $\rho(770)$, $\omega(782)$ or $\phi(1020)$). The scatter takes place between the two hadrons.

In a sizeable fraction of such hadron-hadron interactions, a large rapidity gap in the final state is observed. These 'diffractive' events are attributed to the exchange of an object with the quantum numbers of the vacuum. Within the VMD model, four subclasses of diffractive events (see figure 3.4) are permitted:

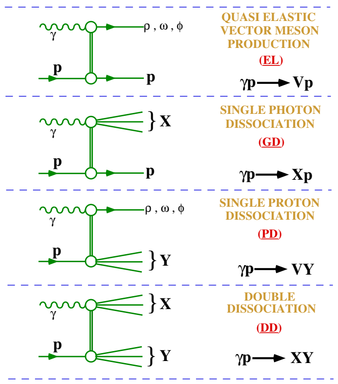

Figure 3.4: *The four subclasses of diffractive events.*

- The VMD elastic process, $\gamma + p \rightarrow V + p$

and inelastic interactions:

- single photon dissociation $\gamma + p \to X + p$
- single proton dissociation $\gamma + p \to V + Y$
- double dissociation $\gamma + p \to X + Y$,

X and Y representing the dissociated photon and proton systems respectively. The compton scattering process, $\gamma + p \to \gamma + p$, is an order higher in α_{em} than the listed processes and can be neglected.

In addition to the diffractive processes, there is a non-diffractive contribution to the VMD cross section, $\gamma + p \to X$, in which no large rapidity gap is seen in the final state, X. The VMD model gives good agreement with low energy data, but fails to predict the outcome of high P_T interactions. To understand such hard interactions QCD is required.

3.5.2 High P_T Interactions

In order to explain the characteristics of high P_T photoproduction, two QCD-inspired classes of interaction are defined [33] (see figure 3.5). If the almost on-shell photon couples directly with the hard subprocess, then the process is referred to as a direct interaction. If the photon interacts hadronically, then the interaction is termed resolved. A useful variable for characterising these processes is x_γ , the fraction of the photon's momentum transferred to the hard subprocess. This will be one for a direct process and less than one for a resolved process.

In the HERA kinematic region, the lowest order QCD matrix elements dominating resolved and direct processes are all exchange diagrams[3]. Photon-gluon fusion ($\gamma g \to q\bar{q}$) dominates the direct cross section while the processes $qg \to qg$ and $gg \to gg$ are responsible for the majority of the resolved cross section [34]. Since

---

[3] a full listing of the LO and NLO processes can be found in tables 4.1 and 4.2.

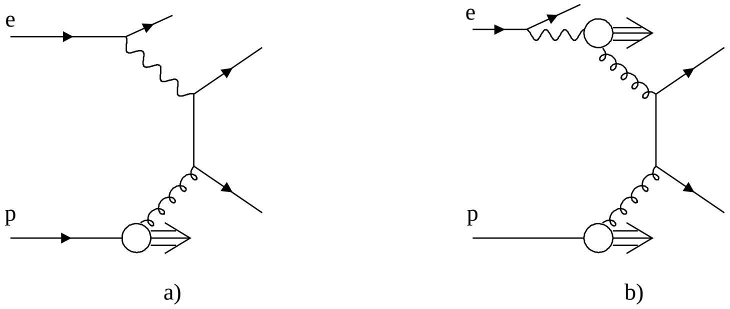

Figure 3.5: *Examples of leading order diagrams for a) direct and b) resolved processes in photoproduction.*

the dominant direct process involves the exchange of a quark and the main resolved processes involve gluon exchange, the dependence of the cross section on the scattering angle in the centre-of-mass frame θ^*, is expected to be different. The quark, being a spin-1/2 particle, results in a $|1 - cos\theta^*|^{-1}$ factor for $d\sigma/dcos\theta^*$ whereas the spin-1 gluon gives rise to a $|1 - cos\theta^*|^{-2}$ dependence. This prediction is well born out by ZEUS measurements [35] (see figure 3.6).

The resolved/direct picture is only valid at lowest order in QCD - at higher orders an ambiguity arises as to how much of the interaction to factorise into structure functions and how much to leave in the hard sub-process [36]. Because of this, care must be taken to use variables which are well defined at all orders but which have natural interpretations in leading order. For example, the definition of x_γ^{OBS} used in equation 3.16 (in which the index i runs over all final state objects, barring the

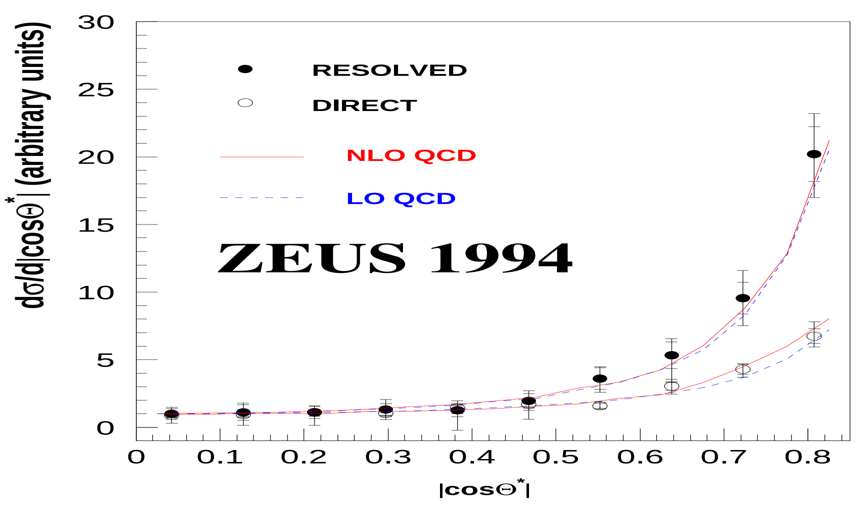

Figure 3.6: *The differential cross section, $d\sigma/dcos\theta^*$, as measured by the ZEUS collaboration. The different $cos\theta^*$ dependence of the resolved and direct event samples is clearly seen and is in good agreement with QCD predictions.*

scattered electron)

$$x_\gamma^{OBS} = \frac{\sum_{jets}(E_{jet} - P_{z,jet})}{\sum_i (E_i - P_{z,i})} \qquad (3.16)$$

reduces to the fractional momentum definition for the lowest order final state, but is well defined, independent of the order of the calculation. Equally importantly, it can be simply implemented experimentally. A useful convention, introduced by the ZEUS collaboration [37], is to divide events into resolved- and direct-enriched samples based on the x_γ^{OBS} of the event, with the former having x_γ^{OBS} <0.75 (see figure 3.7).

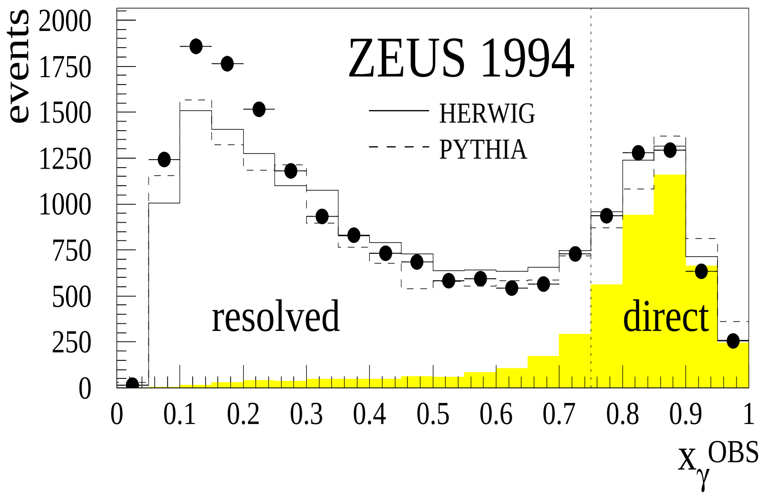

Figure 3.7: *The uncorrected x_γ^{OBS} distribution measured by the ZEUS collaboration, showing the tendency for direct events to lie at high values of x_γ^{OBS} and resolved events at low x_γ^{OBS} .*

Resolved processes include the hard-scattering part of the VMD model, in which a parton from the vector meson interacts with a parton from the proton. A further contribution comes from the 'anomalous' or point-like coupling of the photon to a $q\bar{q}$ pair, which does not form a bound hadron, but instead evolves into a complex hadronic object, a parton from which enters the hard subprocess.

The difference in the event structure of direct and resolved events is striking. In a direct interaction, the entire photon interacts and so the hadronic final state is formed solely from the hard subprocess and the proton remnant. Resolved events however result in a photon remnant which at HERA, due to the large boost in the laboratory system, is thrown into the backward detectors.

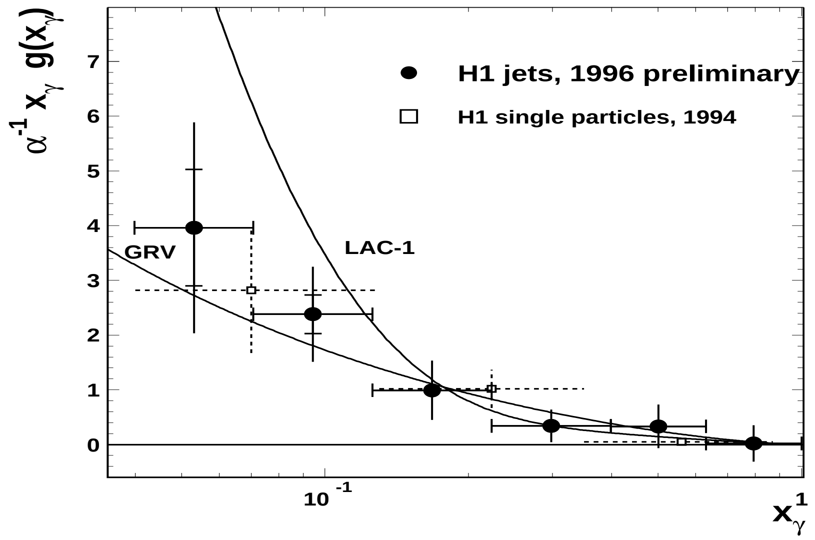

Figure 3.8: *H1 extraction of the gluon density in the photon from 1996 2-jet data [38] and 1994 charged track data [39]. The data are consistent with each other and with the GRV LO parametrisation [40]. The 1996 data rule out the LAC1 [41] gluon parametrisation.*

The high centre-of-mass energies at HERA allow detailed measurements of parton distributions in the photon to be made, using the P_T of the final state hadronic systems (jets) as the probing scale. Similarly, the photon structure function, F_2^γ can be measured directly at e^+e^- colliders [42], with an almost on-shell photon from one of the beam leptons being probed by a highly virtual photon from the other. Although this allows the quark densities in the photon to be well constrained, the gluon density is suppressed, and so obtaining information on it has been difficult. This is not the case at HERA however, and H1 have been able to rule out certain

photon $PDF's$ via a measurement of the gluon density using low P_T^{jet} 2-jet events (see figure 3.8).

For low and intermediate P_T final states (below $\sim$ 30 GeV), the resolved component of F_2^γ is dominant. The direct contribution increases with increasing P_T since high P_T final states require a large subprocess centre-of-mass energy. This drives the kinematics to higher values of x_γ .

Chapter 4

Jet Physics

In the bulk of γp interactions, the momentum transfer between the photon and proton is small. However, in a sizeable fraction of events, a large amount of momentum is transfered, with the result that the outgoing particles leave the interaction point at a considerable angle to the beam axis. In this case, they may be observed in the detector. If the final state particles from the hard subprocess are coloured, then colour confinement results in a group of outgoing hadrons. This group has a typical intrinsic transverse momentum of the hadronisation scale, i.e. ≈ 1 GeV . When the group has a transverse momentum relative to the beam axis much greater than this scale, then a collimated jet of hadrons results. These jets are the footprint of the underlying partonic process and are therefore of great use in understanding the dynamics of partonic interactions.

4.1 Jet Definitions

There is no unique definition of a jet, since jets are not fundamental degrees of freedom of QCD, however a useful jet definition must be [43]:

- Well defined experimentally and simple to measure from the hadronic final state.
- Well defined theoretically and calculable order-by-order in perturbation theory from the partonic final state.
- Closely correlated to the final state quarks and gluons which give rise to the jets.

A further condition which builds on the first two listed above is that the jet definition should be applicable to any stage of the final state, from the hard partons of the subprocess all the way up to the Detector Level[1] objects (for example calorimeter cells or clusters). Since at the lowest order in perturbative calculations, there is a one-to-one correspondence between partons and jets, it is tempting to think of jets as really belonging to an individual parton. This however is untrue at higher orders and jets should always be seen as an event property, albeit one obeying the third point listed above.

4.2 Jet Algorithms

Jet algorithms need to be both collinear-safe and infra-red safe [43]. A divergence appears in the perturbative expansion of a parton cross-section whenever two massless partons are parallel (collinear) or one massless parton has a vanishingly small (infra-red) energy. Both divergences are cancelled in the total cross section by virtual contributions. However, for the jet calculation to avoid the divergences, the treatment of two parallel particles must be identical to the treatment of one with

---

[1] The terms 'Hadron Level' and 'Detector Level' will be used to refer to the event before and after it has passed through the detector respectively. 'Parton Level' implies that the event is considered before hadronisation of the outgoing partons.

the sum of the momenta of the pair. Similarly, the jet must not be affected by the addition of a soft particle.

Exactly the same problems arise experimentally. Two collinear particles will enter the same calorimeter cell and are therefore not resolved, while the infra-red safety requirement is necessary to avoid bias from noise and cell trigger thresholds. Thus, the need for a jet definition to be well defined experimentally and theoretically go hand-in-hand. Traditionally, hadron-hadron and *ep* physics has been analysed using the intuitive approach of cone algorithms [44], whilst e^+e^- experiments have preferred to use clustering algorithms. However, as is pointed out below there are several problems associated with cone algorithms and the trend at hadron colliders in recent years has been towards clustering algorithms as a result [45], [46].

4.2.1 Recombination Schemes

All jet algorithms start with a list of objects (partons, hadrons, calorimeter cells, etc.) and follow an iterative procedure to form jets from these objects (or particles as they will be referred to from now on). The recombination of particles into jets is not unique.

The simplest scheme for recombining particles into jets is to form the jet variables (P_T^{jet} , η^{jet} , ϕ^{jet} , etc.) by four momentum addition. This is known as the covariant E-scheme and results in massive jets. If massless jets are required, then the P_T -weighted scheme is appropriate:

$$E_T^{jet} = \sum_i E_{T,i}, \qquad \eta^{jet} = \frac{\sum_i E_{T,i}\,\eta_i}{\sum_i E_{T,i}}, \qquad \phi^{jet} = \frac{\sum_i E_{T,i}\,\phi_i}{\sum_i E_{T,i}}, \tag{4.1}$$

Since the jets are massless, the rapidity and pseudorapidity of the jets are equivalent, as are the transverse momentum, P_T^{jet} and transverse energy, E_T^{jet} .

Further recombination schemes exist and which to use is largely a matter of taste. In this thesis, the P_T -weighted recombination scheme is used throughout.

4.2.2 Cone Algorithms

Jets in cone algorithms are defined by the direction which maximises the energy flowing through a cone in (η, ϕ) space of radius, R_0 drawn around it. This is a conceptually appealing definition, however as soon as two cones overlap, difficulties develop. The problem is not that different overlap treatments give rise to different results (this is to be expected in dissimilar algorithms). Rather, it is that the addition of soft particles can drastically affect jet properties, violating the infra-red safety requirement and causing large differences between jets defined at the Parton, Hadron and Detector Levels. The problem is shown schematically in figure 4.1, using the Parton Level as an example [47]. In figure 4.1 (a), two partons lie sufficiently far apart to form distinct jets. However, if a soft particle is added between the two partons, as in figure 4.1 (b), then a single jet will be formed if all particles lie within R_0 of the common jet centre.

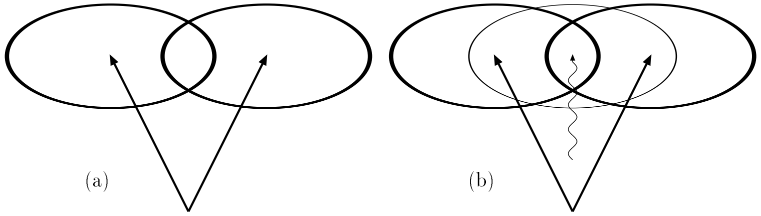

Figure 4.1: *Parton Level illustration of the infra-red safety threat posed by cone algorithms. In (a), there are two hard partons, separated by $> R_0$ but with overlapping cones. In (b) a soft parton has been added in the overlap region.*

The PXCONE algorithm [48] overcomes this problem by considering the midpoint of all pairs of jets as a 'seed' for jet finding. The two hard partons now form a single jet, regardless of whether a soft additional parton is between them. PXCONE is the chosen cone algorithm for this thesis. It has been previously used in many analyses at HERA and is also used at the CDF [49] and OPAL experiments [50]. It operates as follows:

1. Each particle is taken as a jet 'seed', to which steps 2-4 are applied.
2. Equation 4.1 is used to calculate the jet momentum from all particles that fall within a cone of radius R_0 around the seed direction.
3. If the jet and seed directions differ, Step 2 is repeated with the direction of the jet defining the new seed direction.
4. When the seed and jet directions converge, the jet is added to a list of 'protojets', unless it is identical to a previously found protojet, in which case it is thrown away.
5. To ensure infra-red safety, steps 2 to 4 are repeated, using the midpoints of all protojet pairs as seed directions[2].
6. A cutoff parameter ϵ is defined, with protojets of $E_T^{jet} < \epsilon$ being removed from the list.
7. Those protojets remaining which have more than a fraction f of their transverse energy in common with a higher E_T^{jet} protojet are deleted.
8. If a particle is contained in more than one jet, it is removed from all jets save that whose centre is closest in (η, ϕ).

---

[2] In practice, it is only necessary to do this for protojet pairs that lie within a distance of R_0 to $2R_0$.

9. All protojet momenta are recalculated according to equation 4.1, protojets with $E_T^{jet} < \epsilon$ again being removed. All remaining protojets are termed jets.

The reassignment of particles to jets and the recalculation of the jet axis (steps 7, 8) may result in particles assigned to a given jet being greater than R_0 from the jet axis. The parameter settings $\epsilon = 5\,\text{GeV}$ and $f = 0.75$ have been used in this thesis, with two cone radii; $R_0 = 1.0$ and $R_0 = 0.7$.

4.2.3 Cluster Algorithms

Rather than iterating to find a preferred jet direction, cluster algorithms define a closeness parameter for all pairs of particles and successively cluster the nearest particles together until a stopping condition is reached. The JADE collaboration [51] proposed one of the first such algorithms, using invariant mass as the closeness parameter. Although naturally avoiding infra-red and collinear problems (as all clustering algorithms do), low energy particle pairs can have low invariant masses whilst being well separated in angle, leading to single jets being formed from very well-separated particles. To avoid this unphysical clustering, the K_T class of clustering algorithms was proposed [52], in which the closeness parameter is the relative transverse momentum of the softer particle to the harder.

The potential problem of dealing with beam remnants may be avoided by introducing an extra particle of infinite momentum parallel to the incoming beams. Particles being clustered with the infinite momentum particle are excluded from the final state jets. The Longitudinally Invariant K_T algorithm (implemented using the KTCLUS [53] package) belongs to the K_T algorithm family and has the additional advantage of being invariant under longitudinal boosts. It is the default algorithm for this analysis and is detailed below:

1. The algorithm begins with a list of all particles and an empty list of jets.

2. A distance d_{ij} is calculated for every pair of particles and d_i for each particle, according to

$$d_i = E_{T,i}^2 \, R_0^2 \quad \text{and} \quad d_{ij} = \min(E_{T,i}^2, E_{T,j}^2) \, R_{ij}^2 \quad \text{with} \quad R_{ij}^2 = \Delta\eta_{ij}^2 + \Delta\phi_{ij}^2 \, . \tag{4.2}$$

3. $d_{\min}$ is defined as the smallest value of all d_i and d_{ij}.
4. If $d_{\min}$ belongs to the set of d_{ij}, the recombination procedure of equation 4.1 is used to merge particles i and j into a new ‘pseudoparticle’, and i and j are removed from the particle list.
5. If $d_{\min}$ belongs to the set of d_i, the particle i is removed from the list of particles and added to the list of jets.
6. The procedure is finished when the list of particles is exhausted. At this stage, all particles are assigned to a single jet.

This jet definition implies that particles with $R_{ij} < R_0$ are subsequently merged, so that all final jets are separated by distances $R_{ij} > R_0$. The parameter R_0 is set to $R_0 = 1.0$.

Although R_0 sets the size scale for jets in the the PXCONE and Longitudinally Invariant K_T algorithms, it is used in different ways. For the cone algorithm, R_0 is taken from the jet axis, whereas for the cluster algorithm R_0 is the distance scale between particles, regardless of the jet axis.

4.3 Structure of Jet Cross Sections

Inclusive N jet production in ep interactions may be written as

$$e(k) + P(p) \rightarrow e(k') + jet1(E_T^{jet\ 1}, \eta^{jet\ 1}) + ... + jetN(E_T^{jet\ N}, \eta^{jet\ N}) + R \tag{4.3}$$

where k, k' and p are defined in figure 3.1 and R represents the hadronic final state not associated with the hard jets.

In photoproduction, the photon and proton are collinear and so momentum conservation requires a minimum of two (partonic) jets in the final state i.e. $N \geq 2$. As with the DIS cross sections presented in Chapter 3, the photoproduction N jet cross section can be factorised such that

$$\frac{d\sigma_{Njet}(s)}{dy} = \sum_{a,b} \int dx_a dx_b \; f_{\gamma/e}(y) f_{a/\gamma}(x_a) f_{b/P}(x_b) d\sigma_{ab\rightarrow Njets} \tag{4.4}$$

$f_{\gamma/e}(y)$ is defined in section 3.4, while $f_{a/\gamma}(x_a)$ and $f_{b/P}(x_b)$ are the $PDF's$ for partons a and b from the photon and proton respectively. For direct processes, $f_{a/\gamma} = \delta(1 - x_a)$. The physics of the hard subprocess is all contained in the partonic cross section $d\sigma_{ab\rightarrow Njets}$. Thus, only the form of $d\sigma_{ab\rightarrow Njets}$ differs between pure QCD processes and heavy particle production.

4.4 High P_T Jets from QCD Processes

The presence of a hard scale in jet physics (P_T^{jet}) allows a perturbative calculation of $d\sigma_{ab\rightarrow Njets}$. In particular, the dominant contributions to $d\sigma_{ab\rightarrow Njets}$ will come from those diagrams with the least QCD vertices, since each vertex contributes a factor α_s (the perturbative expansion parameter) to the cross section.

There is no one-to-one correspondence between the order of the diagram and the number of partons in the final state. For example, virtual corrections to the Born level diagrams have internal loops. Furthermore, as was pointed out in section 4.1, it is incorrect to assume that a partonic jet is uniquely associated with a single parton. In an order N calculation in α_s, partonic jets are free to contain up to $N - 1$ partons. This means that three parton final states contribute both to the

2-jet and 3-jet cross sections. A complete list of the two and three parton final state subprocesses is given in tables 4.1 and 4.2.

Table 4.1: Two parton final state subprocesses.

direct	resolved		
$\gamma q \to qg$	$qq' \to qq'$	$qq \to qq$	$qg \to qg$
$\gamma g \to q\bar{q}$	$q\bar{q}' \to q\bar{q}'$	$q\bar{q} \to q\bar{q}$	$gg \to gg$
	$q\bar{q} \to q'\bar{q}'$	$q\bar{q} \to gg$	$gg \to q\bar{q}$

Table 4.2: Three parton final state subprocesses.

direct	resolved		
$\gamma q \to qgg$	$qq' \to qq'g$	$qq \to qqg$	$q\bar{q} \to ggg$
$\gamma g \to q\bar{q}g$	$q\bar{q}' \to q\bar{q}'g$	$q\bar{q} \to q\bar{q}g$	$gg \to q\bar{q}g$
$\gamma q \to qq\bar{q}$	$q\bar{q} \to q'\bar{q}'g$	$qg \to qq\bar{q}$	$gg \to ggg$
$\gamma q \to qq'\bar{q}'$	$qg \to qq'\bar{q}'$	$qg \to qgg$	

4.4.1 A Note on Nomenclature

This thesis is concerned with measuring 2-jet and 3-jet cross sections. For 2-jet cross sections, the lowest order (LO) contribution to the cross section comes from $\mathcal{O}(\alpha_s^2)$ processes (figure 4.2 (a)). Next-to-leading order (NLO) corrections come from

processes of $\mathcal{O}(\alpha_s^3)$. The NLO corrections to the 2-jet cross section may be split into real corrections (shown on the left hand side of figure 4.2 (b)), which have three final state partons and virtual corrections (given on the right hand side of figure 4.2 (b)) which come from the interference term between the Born level diagram and diagrams with a single internal loop and two partons in the final state. Therefore, for 2-jet cross sections, LO implies that only $\mathcal{O}(\alpha_s^2)$ processes have been calculated, while NLO includes the $\mathcal{O}(\alpha_s^3)$ processes.

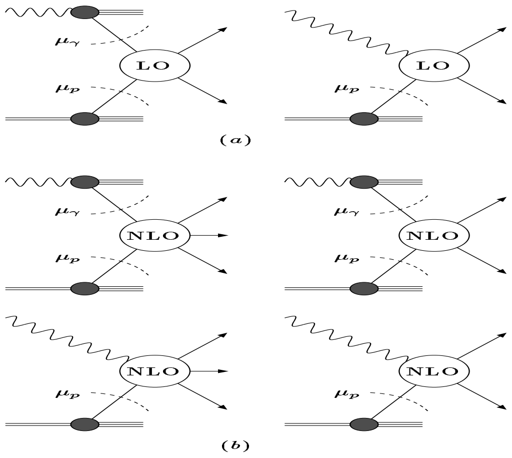

Figure 4.2: *LO (a) and NLO (b) contributions to the 2-jet cross section.* μ_γ *and* μ_p *represent the factorisation scales of the photon and proton respectively.*

For 3-jet partonic cross sections, the lowest order contribution is $\mathcal{O}(\alpha_s^3)$. Therefore, when discussing 3-jet cross sections, LO should be taken to mean $\mathcal{O}(\alpha_s^3)$. $\mathcal{O}(\alpha_s^4)$ corrections to the 3-jet cross section are not yet available.

4.4.2 The 2-jet QCD Cross Section

Because the Born level 2 → 2 subprocess has no dependence on the factorisation scale whereas the $PDF's$ do, LO calculations are subject to large scale uncertainties [36]. However, for three parton final states (the real NLO corrections to the 2 partonic jet cross section), a collinear divergence arises. This divergence is absorbed into the $PDF's$ with the result that the subprocess becomes dependent on the factorisation scale. For example varying μ_F, the photon PDF factorisation scale determines how much of the NLO direct real corrections are factorised into the LO resolved contribution. The scale dependence in the subprocess cancels against that in the $PDF's$ and so reduces the scale dependence of the measured cross section. This cancellation effect is to be expected, for if the calculation is performed to all orders, the scale dependence must vanish, as the exact cross section would then have been calculated and this can have no scale dependence. The reduction of the scale dependence complements the additional accuracy gained by including higher order terms.

In calculating a jet cross section, it is important to work to a consistent order. If the LO cross section is required, then 1-loop α_s and LO $PDF's$ are appropriate. For the NLO case, the 2-loop α_s and NLO $PDF's$ should be used.

4.4.3 The 3-jet QCD Cross Section

The lack of NLO predictions for the 3-jet cross section means that only a LO prediction is possible. Therefore, 1-loop α_s and LO $PDF's$ are used.

4.5 High P_T Jets from Massive Particle Decay

Whereas QCD interactions in photoproduction at HERA are dominated by exchange diagrams, it is also possible for a high mass state to be formed in the subprocess. If such a state decays hadronically, and the decay products have significant transverse momentum, then hadronic jets result. In figure 4.3, the lowest order diagrams for W production are shown [54], as an example of heavy particle production at HERA.

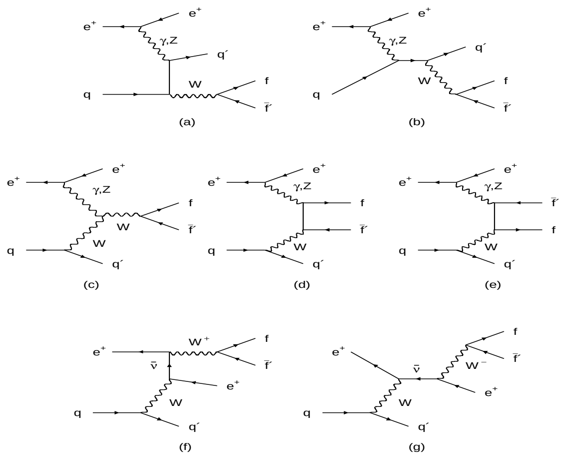

Figure 4.3: *The lowest order diagrams for real* W *production at HERA.*

By four-momentum conservation, the invariant mass of the decay particle jets is equal to the invariant mass of the heavy particle producing them. Therefore, differential cross sections in the invariant masses of jet pairs and 3-jet systems will be sensitive to the production of heavy particles, provided the heavy particle production cross section is not swamped by the QCD cross section.

4.6 Event Generators and Numerical Integration Programs

In this thesis, two types of computer program are used to implement the theoretical predictions and so compare to the measured cross sections. Firstly, there are the event generators (Monte Carlos)[3]. These use a fixed order matrix element calculation (so far only leading order Monte Carlos are available for photoproduction processes) to assign probabilities for each hard subprocess, on the basis of which individual events are constructed. The subprocess is combined with a hadronisation scheme to convert the outgoing partons into observable hadrons. $PDF's$ are used to generate the incoming particles for the subprocess. To supplement the fixed order matrix element calculation, the more sophisticated Monte Carlo programs include initial and final state parton showering. These simulate the dominant higher order terms that the fixed order calculations omit. It should be stressed that although the matrix elements and structure functions are common to all Monte Carlos, the implementation of hadronisation and parton showering differs greatly in different models. Several Monte Carlos have been used in this thesis and they are reviewed below.

The second category of program uses the numerical integration approach. A set of matrix elements are used in conjuction with proton and photon $PDF's$ and an integration over the desired phase space is performed. No attempt is made to convert the outgoing partons into hadrons.

The advantage of a numerical integration program is that it is considerably simpler to add new, higher order matrix elements than is the case with a full blown Monte Carlo event generator. The result is that the order of the calculation in a numerical integration program tends to be higher than in Monte Carlos. However, Monte Carlo programs are extremely useful since, thanks to the hadronisation scheme, observable particles result. This allows direct comparison with experimental Hadron Level cross sections. In fact, in order to compare a numerical integration calculation to data, it is necessary to study the evolution from Parton Level to Hadron Level and this is currently only possible using a Monte Carlo program. Furthermore, by passing the outgoing hadrons from a Monte Carlo through a detailed detector simulation, predictions can be made at the Detector Level. These can then be compared to the Hadron Level predictions in order to estimate the detector's effect on the data. This technique is considered in greater detail in section 5.7.

---

[3] The convention of using the term 'Monte Carlo' to exclusively mean an event generator is used throughout this thesis, even though numerical integration programs (discussed in this section) also use a Monte Carlo approach.

4.6.1 Hadronisation Models

The mechanism by which coloured partons become colourless hadrons is not well understood and different models have been proposed to simulate the hadronisation process. An important feature of any hadronisation scheme is that it is able to fit a wide range of data sets from different colliders without needing to be tuned to each set individually. The two schemes implemented in the Monte Carlo programs used in this thesis are discussed below. Both have been extensively tested at a variety of collider experiments.

String Fragmentation

The JETSET [55] program implements the string fragmentation scheme. Here, coloured partons are connected by a gluon "string" of energy density ~ 1 GeV $/fm$. As the partons move apart, the string stretches and its potential energy increases before breaking to form a $q\bar{q}$ pair. Sufficiently high energy string fragments can form further $q\bar{q}$ pairs. The process continues until only on-shell, colourless hadrons remain.

Cluster Fragmentation

Instead of strings between partons, cluster fragmentation works by splitting all final state gluons into $q\bar{q}$ pairs. Pairs of q's and $\bar{q}$'s then form colourless clusters, with heavy clusters splitting into pairs of light clusters, before all clusters decay into colourless hadrons.

4.7 Photoproduction Event Generators

In this thesis, the Monte Carlo generators PYTHIA [7] and HERWIG [8] are used to simulate photoproduction processes. The principal difference between the Monte Carlos used to generate photoproduction and DIS events is in the treatment of the photon. The DIS Monte Carlos treat the photon as a structureless object whereas the Monte Carlos simulating the photoproduction processes include a photon structure function and a multiple interaction scheme. GRV-LO structure functions are used for the proton and photon in PYTHIA and HERWIG.

4.7.1 Multiple Interactions

So far, only a single hard scatter has been considered in any photon-proton interaction. However, as can be seen from figure 4.4, considerable transverse energy is observed outside the hard jets, this energy being correlated to the x_γ^{OBS} of the event [56].

The additional energy is attributed to 'multiple interactions', MI's, in which partons from the beam remnants interact, giving secondary scatters. This is an area in which theoretical understanding is poor. However, varying the multiple interaction model has been shown to greatly affect the jet rate [57], particularly at low P_T^{jet} . It is

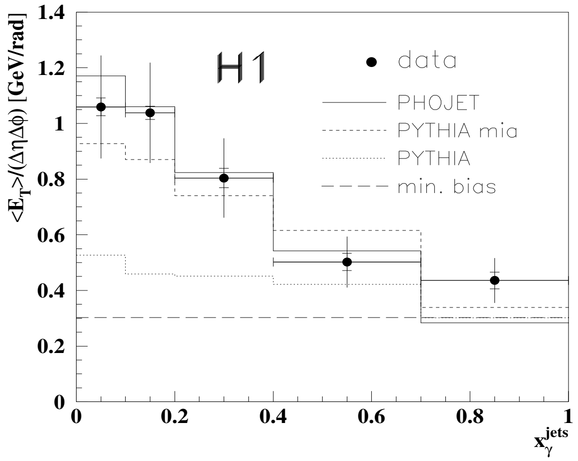

Figure 4.4: *Transverse energy flow outside the jets, as a function of* x_γ^{jets} *(*$\equiv x_\gamma^{OBS}$ *), suggesting the presence of multiple interactions.*

therefore important to model the multiple interactions well. In PYTHIA, a choice of MI models is possible. The model used in this thesis extends the perturbative parton-parton scattering below $\hat{P}_T$, the transverse momentum of the main partonic scatter, to a new limit, P_T^{mi} , set to 1.2 GeV . The divergence as $\hat{P}_T \rightarrow 0$ is regularised and all MI scatters are between gluons and take place independently of eachother. In HERWIG, MI's are simulated by adding low P_T hadrons (the so-called soft underlying event or SUE) to a fraction of the resolved events. The distribution of these hadrons has been tuned to minimum bias $p\bar{p}$ events using data from the UA5 collaboration. A more desirable method than this statistical approach would be to use the JIMMY [58] MI scheme which has recently become available in HERWIG but which was not implemented when the analysis was undertaken.

4.7.2 PYTHIA

The PYTHIA 5.7 event generator is the main Monte Carlo program used in the measurements covered in this thesis. It is run in the photon-proton interaction mode, with the $e \to e\gamma$ vertex being simulated separately, using equation 3.15. Events were generated over all y, with Q^2_{max} =4 GeV^2 . In addition to the leading order cross section coherent, virtuality ordered initial and final state parton showering is included. Resolved and direct processes (including charm and bottom boson-gluon fusion production) were generated separately. For each, two samples were created, one with a transverse momentum cutoff for the hard subprocess, $\hat{P_T} > 6$ GeV and another (of significantly greater luminosity) with $\hat{P_T} > 17$ GeV . By merging these two samples, high Monte Carlo statistics were guaranteed in all measured bins whilst ensuring that the poor correlation between $\hat{P_T}$ and P_T^{jet} does not cause an underestimation of events with low P_T^{jet} .

Multiple interactions were included for all resolved processes. This procedure has recently been found to be flawed, in that only VDM processes should be subjected to multiple interactions and not the anomalous contribution [59]. However, the energy flow outside the jets, averaged over the entire PYTHIA event sample, is seen to model the data well even with this error (see figures 5.13 and 5.14). 1 loop α_s is used with 5 flavours, with Λ_{QCD} taken from the proton PDF , i.e. $\Lambda^{[4]}_{QCD}$ =200 MeV. String hadronisation is implemented using the JETSET program.

4.7.3 HERWIG

The hard subprocess in HERWIG is similar to that in PYTHIA, however particular attention has been paid to parton showering in HERWIG, with a complete, coherent showering algorithm applied to initial and final state radiation. HERWIG events were generated over the same kinematic range as the PYTHIA sample, with $\hat{P_T} > 6$ GeV and $\hat{P_T} > 17$ GeV samples again being created separately. Resolved and direct processes were generated individually, with 20% of the resolved events subject to an additional SUE, as described in 4.7.1. A 2-loop α_s was used[4] with 5 flavours and $\Lambda^{[5]}_{QCD} = 200$ MeV (which corresponds at 2-loop order to $\Lambda^{[4]}_{QCD}$ =291 MeV). To hadronise the outgoing partons, HERWIG uses the cluster fragmentation model.

4.8 Massive Particle Decay Event Generator

4.8.1 EPVEC

The EPVEC [60] program is based upon PYTHIA, but additionally includes the lowest order diagrams for W production (figure 4.3). However, in the version used, the full power of PYTHIA is not available. In particular, parton showering is not included. EPVEC is only used in this thesis to estimate the W production contribution to the measured cross sections.

4.9 DIS Event Generators

To model the background from DIS events, the following two event generators were used. Both were interfaced to the HERACLES [61] program, which simulates QED radiation from the incident and scattered electron.

---

[4] This is inconsistent with the use of leading order $PDF's$ but consistent with parton showering, which simulates higher order processes. The order of α_s to use in a leading order matrix element, parton shower Monte Carlo is not clear. A discussion of the effect on the cross section predictions from using 1-loop and 2-loop α_s is given in section 6.3.

4.9.1 RAPGAP

NC DIS events with $Q^2 > 4$ GeV^2 were generated using RAPGAP 2.3 [62] with CTEQ4M parameterisations for the proton (a structureless photon is assumed). Parton showering is implemented by the JETSET program. RAPGAP was used rather than DJANGO [63], since the latter was found to greatly overestimate the low Q^2 2-jet rate.

4.9.2 DJANGO

As a large statistics charged current sample generated by the RAPGAP Monte Carlo was not available, the DJANGO 6.2 Monte Carlo was used with parton showering performed using the Colour Dipole Model as implemented in the ARIADNE [64] program. Despite the overestimation of the 2-jet rate that results, the CC background was found to be negligible in all bins.

4.10 Numerical Integration Programs

4.10.1 JetViP

The JetViP 1.1 [9] computer program uses the full $2 \to 2$ matrix elements plus the real and virtual corrections to make next-to-leading order (NLO) predictions of the 2-jet partonic cross section and leading order (LO) predictions of the 3-jet partonic cross section in photoproduction (and DIS if required). Contributions from resolved and direct processes were calculated separately. The VEGAS [65] package was used to perform the integration over the allowed phase space with five iterations to ensure stability. Divergences in the real and virtual corrections are handled by JetViP using the phase-space slicing approach. Each cross section bin was calculated separately, with 50000 integration points used for the LO cross sections and 500000 points for the NLO cross sections. As a result, statistical errors were less than 2% in all bins. For the NLO jet cross sections, 2-loop α_s with 5 flavours was used and GRV-HO $PDF's$ chosen for the proton and photon, whilst for the LO cross sections, 1-loop α_s with 5 flavours and GRV-LO $PDF's$ were used. JetViP contains no parton showering or hadronisation model.

Chapter 5

High P_T Jet Cross Section Measurements

5.1 Motivation

In a recent H1 publication [66], an excess of events with a high P_T isolated lepton accompanied by large missing transverse momentum, $P_{T,miss}$ was observed (figure 5.1). These events may be interpreted in terms of the leptonic decay of a heavy particle. In particular three of the events are consistent with W production (see figure 4.3), albeit with a larger than expected cross section. Attempts have been made to interpret the remaining three muon events, for example as the signature of single top production [67]. To properly investigate the hypothesis that a heavy particle decaying leptonically is responsible for these events, it is important to consider other decay channels.

In the leptonic events the large $P_{T,miss}$ is consistent with the presence of an undetected neutrino. Taking W production as an example of a heavy particle decay, the charged lepton and neutrino would be the decay products of the W. In the hadronic decay channel, the W instead decays to two high P_T quarks. Thus, in addition to the jet produced by the struck quark, two further jets may be expected, and no significant $P_{T,miss}$. The advantage of looking in the hadronic decay channel is that no information is lost, as is the case with the undetected neutrino in leptonic decays. However, there is a serious disadvantage: the QCD production of multijet events is expected to swamp the signal from heavy particle decays. If heavy particle decays are to be separated from this ‘background’, then QCD multijet production must be well understood. This provides a second motivation for the measurements, since they test the validity of QCD up to the highest energies available in the photoproduction

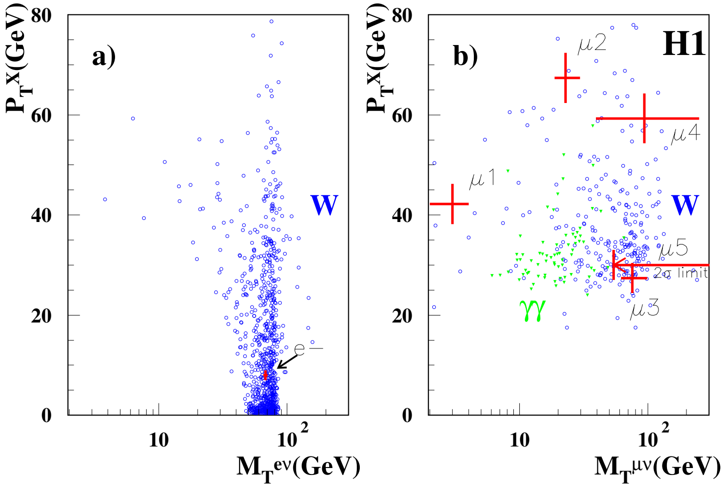

Figure 5.1: *Distribution of the observed H1 isolated lepton events in the transverse momentum of the hadronic system, P_T^X versus the transverse mass of the leptonic system, $M_T^{l\nu}$: a) electron channel; b) muon channel. The dominant Standard Model contributions (open blue circles for W production, green triangles for photon-photon processes in the muon channel) are shown for an accumulated luminosity 500 times higher than in the data.*

environment at HERA.

To this end a sample has been defined, requiring at least two hard jets. A subsample, requiring a third hard jet, is then constructed. From these samples, differential 2-jet and 3-jet *ep* cross sections in jet transverse momentum and invariant mass are evaluated.

5.2 Event Selection

In order to reduce the enormous number of events down to a reasonably sized event sample, whilst retaining all events of interest, several tiers of cuts have been used. For each event, the first step is to check that the high voltage of all required subdetectors are at the nominal settings. The subdetectors used are CJC1, CJC2, CIP, COP, SpaCal, the Liquid Argon Calorimeter (EMC and HAC), the Luminosity System and the Time of Flight System.

The next stage is to select events with a jet structure. This is achieved by using the Level 5 photoproduction jets class (Class 20), defined during the L5 Event Classification (see section 2.7). The criteria for an event to belong to Class 20 are as follows:

- No subtrigger consistent with a SpaCal calibration event is set.
- There is exactly one primary reconstructed vertex, and this vertex is required to be in the range

  $$-40\text{cm} < z(\text{primary vertex}) - z(\text{nominal interaction point}) < 50\text{cm} ,$$

  so reducing the non-*ep* background.

- The number of upstream tracks, N_{up} must be fewer than the number of tracks pointing[1] to the vertex, N_{vtx} unless $N_{vtx} < 4$. In this case, N_{up} must be less than four.
- At least one of the following must be satisfied:
  - the total transverse energy, calculated from calorimeter cells, $E_T^{tot} >30$ GeV
  - the transverse energy of the first[2] jet, $E_{T,1} >10$ GeV
  - the transverse energy of the second jet, $E_{T,2} >7$ GeV
  - the pseudorapidity of the most backward going jet $<$ -1.5 .

Jets are found using calorimeter cells as input objects and using a basic (non-infrared safe) cone algorithm. This would not be a sensible algorithm to use for an analysis (see section 4.2) however it is valid for selecting events, prior to the final analysis cuts. As will be seen from subsection 5.4.1, the final analysis cuts require jets with considerably higher E_T (albeit using a different jet algorithm) than the jet cuts above so no bias is introduced by the Class 20 jet selection.

5.2.1 The Hadronic Final State Reconstruction

At this stage, most non-*ep* background has been removed. It now becomes important to reconstruct the hadronic final state (HFS) in a way that best mimics the event structure prior to interaction with the detector. For data, only the Detector Level is known. However, studying the effect of going from the Hadron Level to the Detector Level using Monte Carlo events allows a correction to be made to the data so that

---

[1] 'Pointing' is defined as the track having a distance of closest approach (dca) less than 3cm from the reconstructed event vertex and the z coordinate of the dca point, z_{dca} being less than 20cm from the z coordinate of the vertex, z_{vertex}.

[2] Since the jets are ordered in P_T^{jet} throughout this analysis, the 'first' jet refers to the highest P_T or 'leading' jet, the 'second' jet to the second highest P_T jet and so forth.

Hadron Level data distributions can be produced. This procedure is described in more detail in Section 5.7.

There are several ways in which the HFS may be reconstructed from the detector information. The H1 reconstruction software converts hits in the trackers into tracks and energy deposits in the calorimeter cells into clusters. Using these tracks and clusters, the following methods may be employed to form the HFS.

- *Only the tracking information may be used.* This method is most frequently used in Heavy Flavour physics and in charged particle multiplicity studies. However, it is inappropriate for a jet analysis since much of the energy in a jet is carried by neutral particles and charged particles may be of too high energy for their track curvature to allow an accurate momentum measurement.
- *Only the calorimeter information is used.* This method is often adopted for jet studies, since the majority of the energy of the jet is carried into the calorimeters and it is simpler to implement an analysis with as few detector components as possible. However, particles giving rise to low energy, curved tracks tend to be well measured in the trackers while the energy resolution of such particles in the calorimeters is poor. Combining tracker and calorimeter information improves energy resolution and therefore improves the accuracy of the measurement.
- *Both tracking and calorimetry information is used.* This is the method chosen for this thesis.

Since the Hadron Level must be insensitive to the choice of HFS reconstruction, a study has been undertaken in order to understand the effects of using calorimeter clusters rather than combined (COMB) track/cluster objects. The change in the cross section is below 10%, significantly less than the uncertainty associated with the LAC energy scale. A dead material correction is applied when constructing COMB objects.

5.2.2 Electron Finding

In order to select photoproduction events, it is necessary to anti-tag electrons in the main calorimeters. To find backward-going electrons that would enter the SpaCal, a cut is made on y, reconstructed according to the Jacquet-Blondel method,

$$y_{JB} = \frac{\sum_i (E_i - P_{z,i})}{2E_e}. \tag{5.1}$$

The index in equation 5.1 runs over all hadronic final state objects. E_e is the electron beam energy (27.6 GeV). Subsection 5.4.2 describes the use of this cut in removing NC DIS events.

In the LAC, NC DIS rejection is achieved by running the default H1 electron finding algorithm, QESCAT. This algorithm combines track and cluster information and flags events where an object consistent with an electron is found. Many parameters exist for this algorithm and the default settings were used for each. The minimum energy of an electron candidate was set to 9 GeV.

5.2.3 Subtriggers

Inevitably, the H1 trigger system rejects a small proportion of ‘good’ *ep* events as well as non-*ep* background. By understanding the efficiency of the trigger, this undesirable effect can be accounted for by reweighting the data appropriately. The procedure followed is to select events only if one or more of a set of (L4) subtriggers fired and to calculate the efficiency of each subtrigger. The four subtriggers chosen (s64, s67, s75 and s77) all require energy deposits in the LAC. Each requires a different criteria in order to fire and so by using all four, more events are selected than would be the case if only one was chosen. In addition to the LAC requirement, there are also vertex and timing requirements on these triggers. Figures 5.3 and 5.4 show that when inefficiencies arise, they are caused predominantly by the LAC requirement.

The efficiency is found by selecting events using an independent subtrigger (the monitor subtrigger) and looking at the fraction of these events that fired a subtrigger used in the analysis. Thus, the analysis subtrigger efficiency, $\eta_{s/t}$ is defined by

$$\eta_{s/t} = \frac{N(monitor\ subtrigger\ AND\ analysis\ subtrigger\ fired)}{N(monitor\ subtrigger\ fired)} \qquad (5.2)$$

where $N(x)$ is the number of events fulfilling condition x.

For a subtrigger to be used as an independent monitor, it must have no conditions in common with the analysis subtrigger but still select events which would pass the analysis cuts. No such subtrigger existed in the data-taking period used in this thesis. The subtrigger s3 required only that significant energy be deposited in the electromagnetic SpaCal[3] and is therefore independent of the analysis subtriggers used. However, the full analysis cuts would kill events passing s3 because of the y_{JB} cut. This cut is therefore relaxed in the subtrigger efficiency study.

The price paid for adopting this approach is that the kinematics of events in the monitor sample and analysis sample are different. The monitor sample consists of high P_T 2-jet DIS events where the electron enters the SpaCal and deposits significant energy. This biases the sample to low y and so the events are thrown forward in the laboratory frame. The pseudorapidity spectrum of the jets will therefore be affected. In order to ensure that this does not bias the trigger efficiency study, the jet pseudorapidities for the monitor and analysis samples were compared and the monitor sample reweighted in the leading jet pseudorapidity to mimic the analysis sample. The trigger efficiencies before and after reweighting can be seen in figure 5.2. Although no bias is observed, a systematic error is applied in Section 5.8 which reflects the uncertainties associated with this reweighting procedure.

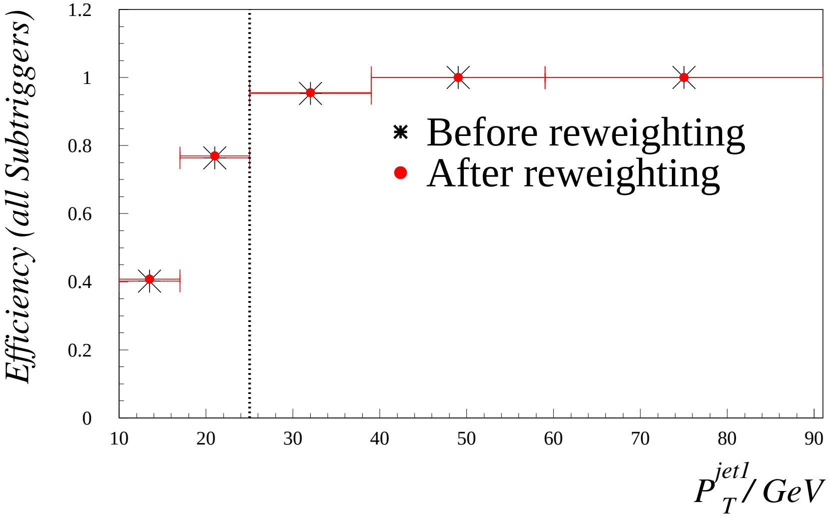

Figure 5.2: *The total combined subtrigger efficiency before and after reweighting the monitor trigger sample. The difference between the two sets of points is negligible in all bins. The dashed line represents the cut on leading jet* P_T .

In figures 5.3 and 5.4, the trigger efficiencies for the final data sample are shown for the leading jet transverse momentum, P_T^{jet1}. It can be seen that the efficiency is always higher than 95% above the final P_T^{jet} cuts. The inefficiencies at low P_T^{jet} are seen to arise from the LAC requirement. The rise from low to high efficiency in each subtrigger reflects the energy thresholds of each LAC trigger component.

---

[3] s3 also has some timing requirements which are present in the analysis subtriggers. However, all the timing conditions have been shown to be almost 100% efficient in previous jet analyses.

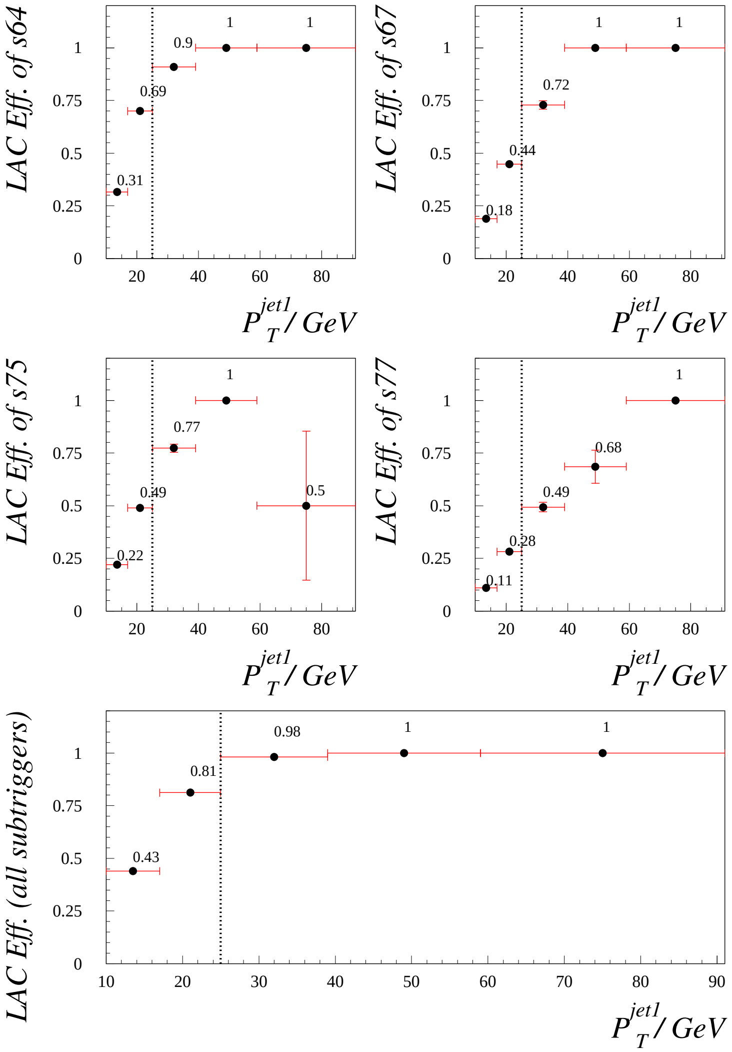

Figure 5.3: *The subtrigger efficiencies for the LAC component of each subtrigger used in this thesis, and the combined LAC requirement efficiency for all four subtriggers, binned in the leading jet P_T . The dashed line represents the cut on leading jet P_T .*

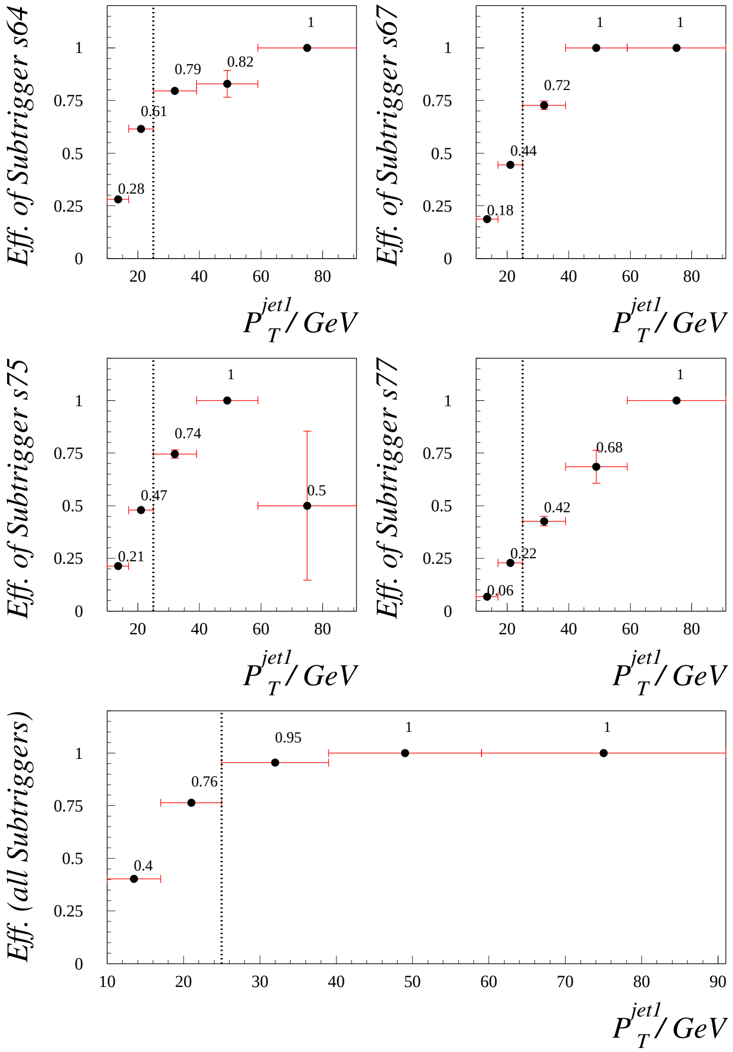

Figure 5.4: *The total subtrigger efficiency for each subtrigger used in this thesis, and the combined efficiency of all four subtriggers, binned in the leading jet P_T . The dashed line represents the cut on leading jet P_T .*

5.3 Jet Calibration

When particles pass through the detector, some energy is lost during interactions with dead material. While attempts are made to correct for this effect by calibrating each wheel and octant of the LAC, a residual difference between the Hadron and Detector Level jets remains. From figure 5.5, it can be seen that the energy loss at the Detector Level varies with jet polar angle, θ_{Jet}. No significant variation with P_T^{jet} is observed.

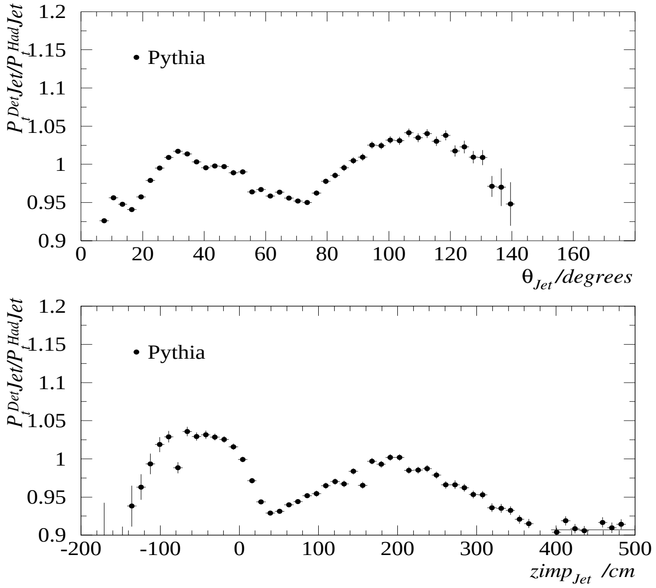

Figure 5.5: *The ratio of P_T^{jet} between Detector and Hadron Level for PYTHIA events passed through the H1 detector simulation, as a function of the jet polar angle, θ_{Jet} and z-coordinate of the jet's impact on the LAC, $zimp_{Jet}$. The $zimp_{Jet}$ plot shows the effect more clearly since the θ_{Jet} plot is smeared by the z-vertex distribution.*

The P_T^{jet} of each jet in data and Monte Carlo is rescaled as a function of $zimp_{Jet}$, using a fit to the distributions in fig 5.5. The resolutions between Hadron and Detector Levels, after all cuts have been applied (see Section 5.4) for P_T^{jet} , η^{jet} , the invariant mass of the two highest P_T^{jet} jets, M^{12} and the invariant mass of the three highest P_T^{jet} jets, M^{123} are shown before and after rescaling in figures 5.6 and 5.7 respectively.

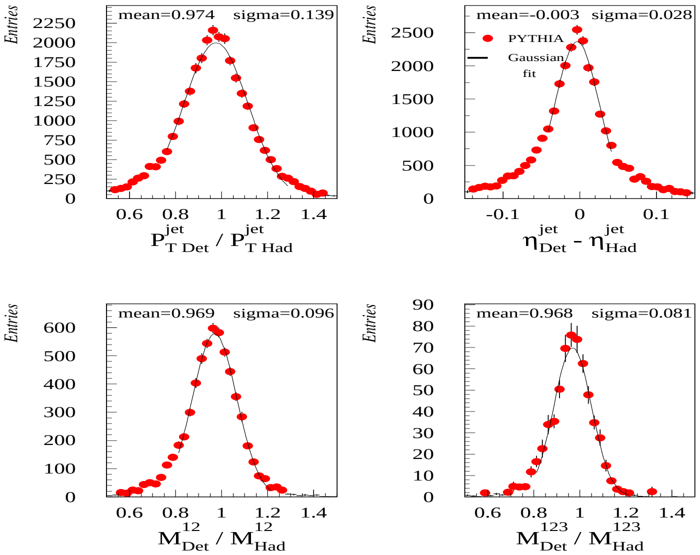

Figure 5.6: *The P_T^{jet} , η^{jet} , M^{12} and M^{123} resolutions for PYTHIA between jets at the Hadron and Detector Level before applying the pseudorapidity-dependent P_T^{jet} rescaling.*

While the η^{jet} resolution is not affected by the rescaling, Gaussian fits to the P_T^{jet} , M^{12} and M^{123} resolutions show that the mean of the resolutions are closer

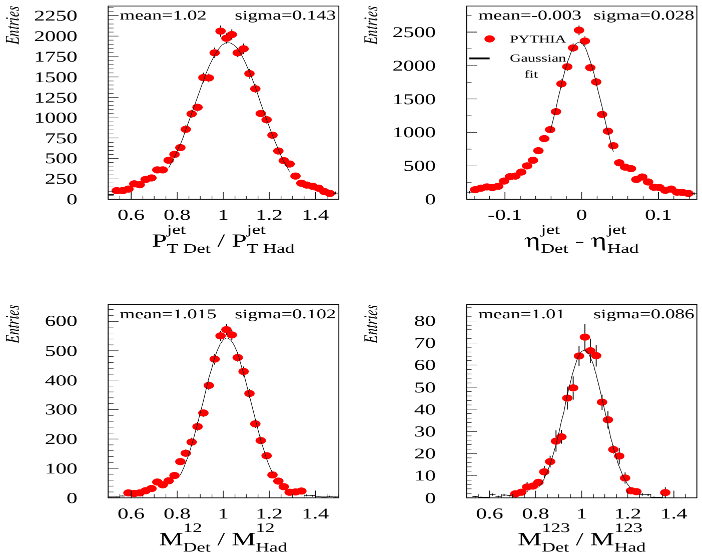

Figure 5.7: *The* P_T^{jet} *,* η^{jet} *,* M^{12} *and* M^{123} *resolutions for PYTHIA between jets at the Hadron and Detector Level after applying the pseudorapidity-dependent* P_T^{jet} *rescaling.*

to unity after rescaling, which was the aim of the rescaling procedure. The width (sigma) of the distributions is not significantly affected by the rescaling.

5.4 Fiducial Cuts

In this thesis, very high P_T^{jet} systems are required whereas the majority of events in Class 20 are at relatively low jet P_T . Furthermore, it was found that even after requiring high P_T jets, a significant background remains from neutral current DIS events, both at low Q^2 , where the electron enters the SpaCal and the hadronic final

state forms a 2-jet system, and at higher Q^2 where the scattered lepton is misidentified as a jet in the LAC. Subsection 5.4.1 considers the cuts used to isolate the high P_T jets while subsection 5.4.2 focuses on the anti-DIS cuts applied. Subsection 5.4.3 reviews the cuts used to define the Hadron Level cross sections.

5.4.1 Jet and Kinematic Cuts

Following the discussion in section 4.2, the Longitudinally Invariant K_T algorithm with P_T recombination scheme was chosen for this analysis (see appendix A for a comparison of results obtained using cone and cluster algorithms). For each event, the following criteria were required (P_T^{jetN} refers to the P_T of the Nth highest P_T jet in the event).

- at least one high quality track must point to the interaction vertex.
- -36cm $< z_{vertex} <$ 34cm.
- $P_T^{jet1} > 25\ \ GeV$.
- $P_T^{jet2} > 15\ \ GeV$.
- for the 3-jet sample only, $P_T^{jet3} > 10\ \ GeV$.
- The pseudorapidity of each jet, η^{jet} is restricted to $-0.5 < \eta^{jet} < 2.5$. All jets are then well contained in the LAC.
- A cut on missing transverse momentum, $P_{T,miss} <$ 20 GeV is used to remove charged current and cosmic ray events.

The choice of an asymmetric cut on the P_T^{jet} of the top two jets is justified in appendix B.

	2-jet Sample	3-jet Sample
PYTHIA Scale Factor	1.13	1.19
HERWIG Scale Factor	2.23	4.63
Number of Data Events	6466	961

Table 5.1: Scale factors required to match the number of events seen in the data (with all cuts imposed) for the 2-jet and 3-jet samples of each photoproduction Monte Carlo.

Figure 5.8 shows some important distributions for data and Monte Carlo, after applying all the above cuts, save the cut on $P_{T,miss}$. The $P_{T,miss}$ cut is relaxed in order to show the distribution in the excluded region. Although a significant NC DIS background remains, the data distributions are well modelled by the combination of photoproduction and neutral current Monte Carlos. The normalisation of the PYTHIA and HERWIG samples has been scaled to match the number of events seen in the data, after applying all cuts and correcting to the Hadron Level.[4]. The scale factors are given in table 5.1.

5.4.2 Anti-NC DIS cuts

The final stage of the cut procedure is to remove the NC DIS events in the sample (CC interactions have a considerably lower cross section than NC DIS interactions and besides, are removed by the $P_{T,miss}$ cut). The following cuts against NC DIS events are implemented.

---

[4] Since HERWIG and PYTHIA have different correction factors (see section 5.7) and the data are corrected to the Hadron Level using PYTHIA, the HERWIG distributions at the Detector Level are not exactly matched in normalisation to the data.

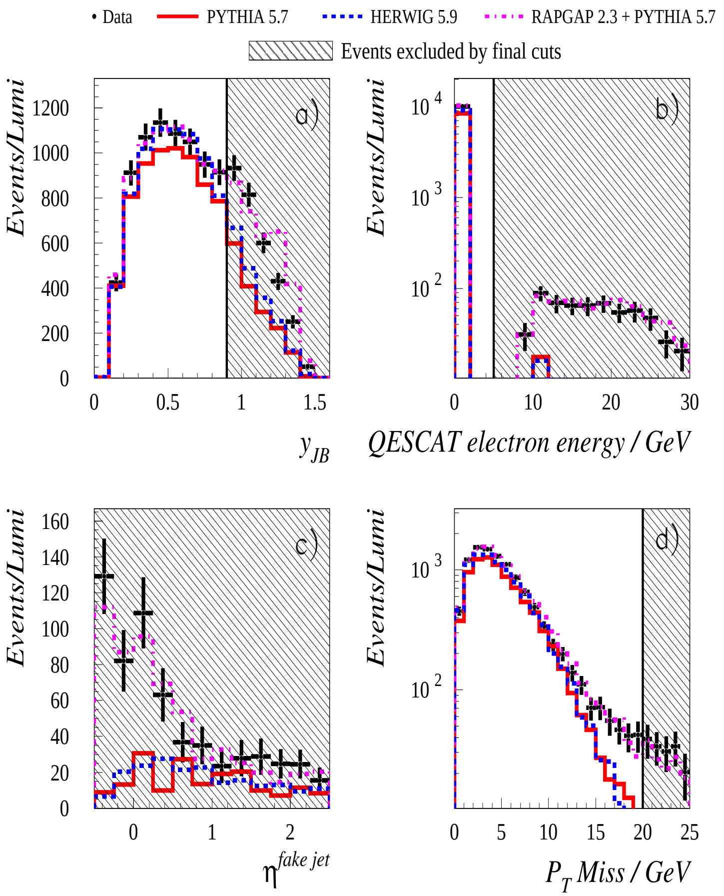

Figure 5.8: *The a) y_{JB} , b) energy of the LAC electron, c) η^{jet} of the LAC electron faking a jet and d) $P_{T,miss}$ distributions in data, PYTHIA, HERWIG and PYTHIA+RAPGAP after the jet cuts have been applied. The $P_{T,miss}$ cut is relaxed for these figures. Events in the hatched area are killed when the full set of cuts (including NC DIS rejection) are applied.*

- y_{JB} <0.9

  Low Q^2 NC DIS events are mostly found at $y_{JB} \simeq 1$. The electron scatters into the SpaCal and is included in the hadronic final state. The sum in equation 5.1 is then over all final state particles and by energy and momentum conservation, is forced to equal twice the electron beam energy. Cutting at y_{JB} <0.9 removes these events.

- *No QESCAT electron.*

  Figure 5.8 b) shows the QESCAT electron energy spectrum. At high Q^2 , the data normalisation and shape are well modelled by the RAPGAP Monte Carlo, giving confidence in the QESCAT algorithm and justifying the removal of these events.

- *Removal of events where LAC electron fakes a jet.*

  Since the QESCAT electron finder is not 100% efficient at finding electrons, some high Q^2 events pass all the above cuts, with the electron being scattered into the LAC and faking a jet. Events are rejected when a jet has an isolated track[5] close to its centre (within 0.5 units in (η, ϕ) space) and at least one of the following criteria are met:

  - greater than 90% of the energy of the jet is deposited in the EMC.

  - the energy profile within the jet is highly collimated. Two cones are defined in (η, ϕ) space with the jet axis defining the cone centre. The inner cone has a radius of 0.2 and the outer cone a radius of 0.5. The energy of all clusters within each cone is summed. If greater than 90% of the energy of the outer cone is also found in the inner cone, the energy profile is defined as 'highly collimated'.

  - the track points towards a known LAC crack. Cracks exist between LAC wheel octants (ϕ cracks) and where LAC wheels meet (z cracks). Events are excluded when the ϕ coordinate of the isolated track is within 2° of a ϕ crack in the LAC barrel. ϕ cracks occur every 45° around the LAC, due to its octant structure.

  Such configurations most frequently arise when an electron has faked the jet.

---

[5] An isolated track is defined as one separated from all other tracks and clusters by more than 0.5 units in (η, ϕ) space.

After applying the full cuts, the distributions in figure 5.9 are obtained. All backgrounds have been reduced to an acceptably low level and the shapes of both PYTHIA and HERWIG are in good agreement with the data. The scale factors in table 5.1 have again been applied.

In figure 5.10, a display of a typical 2-jet event is shown. The two well-separated large energy deposits forming the 2-jet system are clearly visible. A high mass 3-jet event is shown in figure 5.11. Whereas the 2-jet event has a back-to-back structure, the third jet in figure 5.11 (seen between the two leading jets in the lego plot) causes the two leading jets to be less than 180° apart in the $r-\phi$ plane.

5.4.3 Hadron Level Cuts

The cuts required to define the Hadron Level sample are analogous to those at the Detector Level. The P_T^{jet} and η^{jet} cuts are identical and the only other cuts used are Q^2 <4 GeV^2 and y <0.9. The Q^2 cut restricts the cross section to the untagged photoproduction regime while the y cut mimics the y_{JB} cut at the Detector Level.

5.5 Event yield

In order to check that the event selection is stable over the entire data taking period, the number of events selected per unit luminosity as a function of HERA luminosity

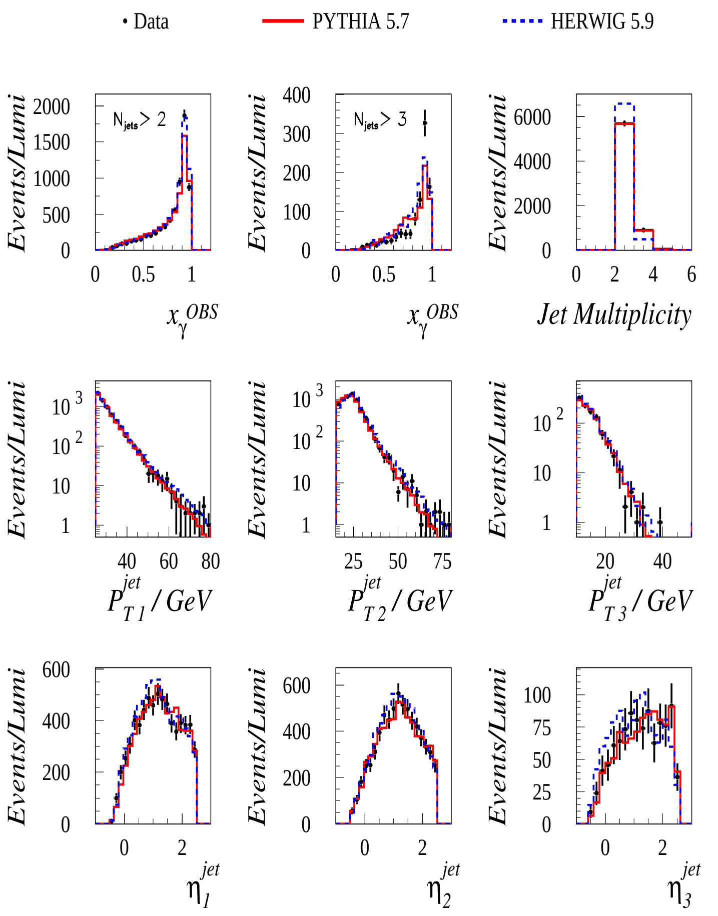

Figure 5.9: *Important distributions after all cuts have been applied. The two* x_γ^{OBS} *plots differ by the number of jets required. The poor description of the jet multiplicity by HERWIG is discussed in section 6.3. PYTHIA and HERWIG have been scaled by the factors given in table 5.1.*

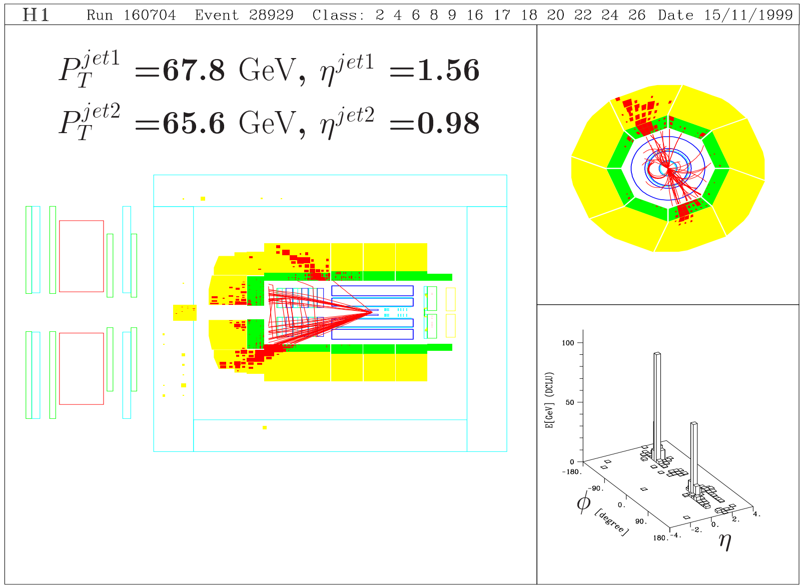

Figure 5.10: *An example of a high* P_T^{jet} *2-jet event, passing all of the analysis cuts. The three views shown are (clockwise from top right) a slice through the* $r-\phi$ *plane, a lego plot of cluster energy as a function of pseudorapidity and azimuthal angle and a slice through the* $r-z$ *plane.*

run was plotted for each year, 1994 to 1997. The results are shown in figure 5.12. The means for each year are consistent with an event yield which is independent of the HERA luminosity run, as required.

5.6 Jet Profiles

In Section 4.7.1, the need to accurately model the energy flow outside the jets was highlighted. Jet profiles are a powerful way of checking that the energy flow is

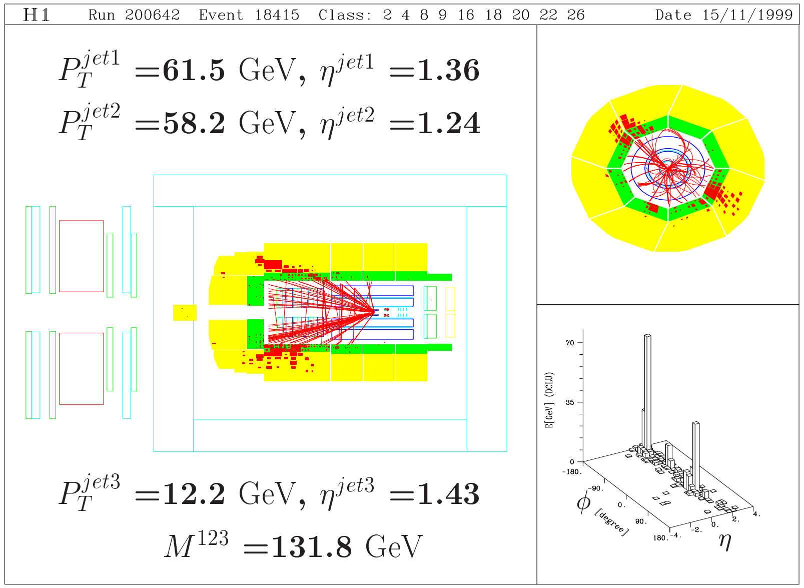

Figure 5.11: *An example of a high mass 3-jet event, passing all of the analysis cuts. The three views shown are (clockwise from top right) a slice through the $r-\phi$ plane, a lego plot of cluster energy as a function of pseudorapidity and azimuthal angle and a slice through the $r-z$ plane.*

well described. A jet profile is built up by plotting the transverse momentum of all HFS objects in the event as a function of their distance from the jet axis. To obtain a pseudorapidity jet, η^{jet} (azimuthal angle, ϕ^{jet}) profile, the difference in pseudorapidity (azimuthal angle) between the jet axis and each HFS object is used. The η^{jet} and ϕ^{jet} profiles for PYTHIA with multiple interactions and HERWIG with 20% Soft Underlying Event are shown in figures 5.13 and 5.14. Both event generators model well the energy flow inside and outside the jet.

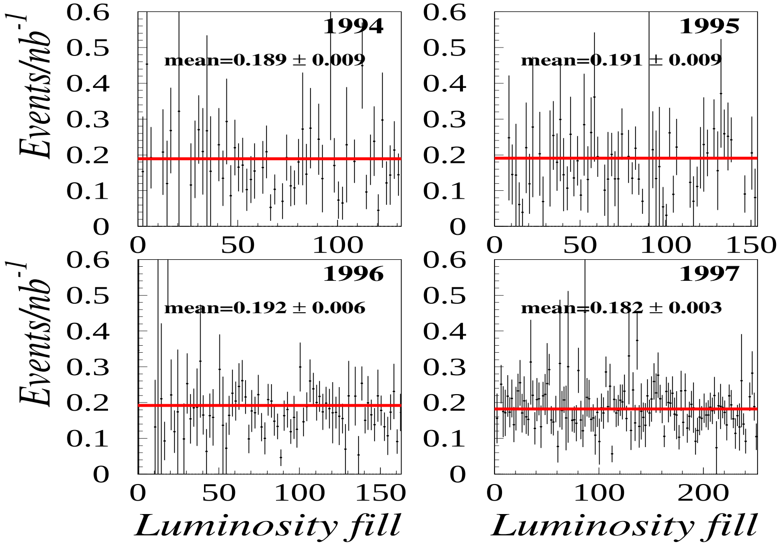

Figure 5.12: *The number of events selected per unit luminosity as a function of HERA luminosity fill in the years 1994 to 1997. The horizontal red line denotes the year average. To aid clarity, only luminosity fills with an odd fill number are plotted.*

5.7 Correcting for Detector Effects

Since Hadron Level photoproduction cross sections are required, backgrounds are subtracted and the effects of the H1 detector removed. This is done via a bin-by-bin acceptance correction, defined by equation 5.3,

$$\sigma_i = \frac{N_i^{Data}/\epsilon_i - N_{i,Bkg}^{Det}}{\mathcal{L}A_i} \qquad (5.3)$$

where the subscript i denotes the i^{th} bin of the cross section σ, ϵ is the trigger efficiency, N^{Data} is the number of data events and N_{Bkg}^{Det} is the number of background

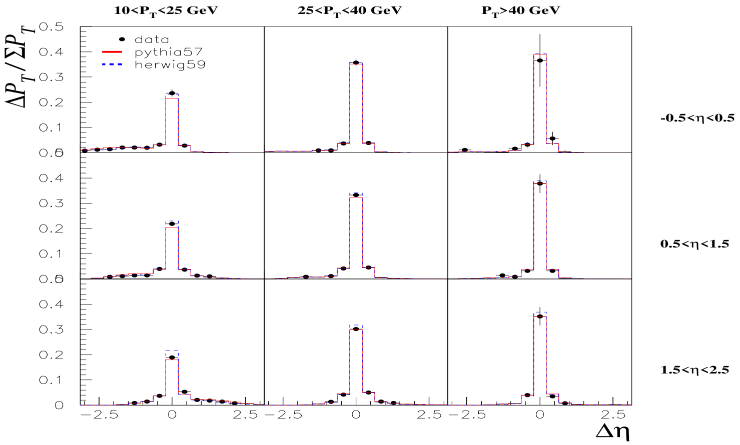

Figure 5.13: *The pseudorapidity jet profile, split into regions of* P_T^{jet} *and* η^{jet}. *The vertical axis shows the summed scalar transverse momentum,* ΔP_T *in each bin divided by the summed scalar transverem momentum,* ΣP_T *of all HFS objects.*

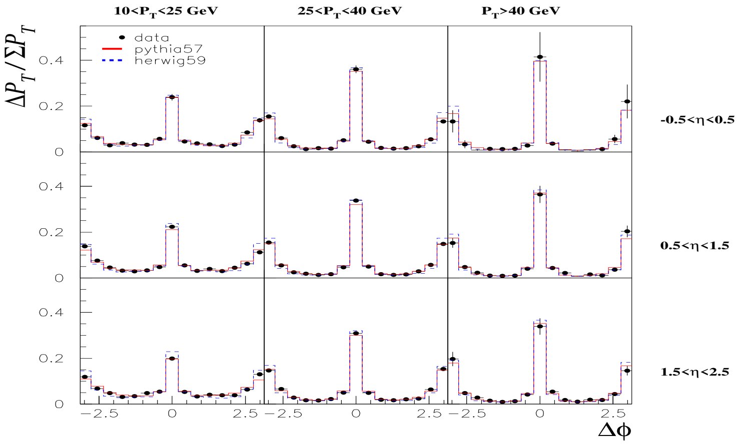

Figure 5.14: *The azimuthal angle jet profile, split into regions of* P_T^{jet} *and* η^{jet}. *The vertical axis shows the summed scalar transverse momentum,* ΔP_T *in each bin divided by the summed scalar transverem momentum,* ΣP_T *of all HFS objects.*

(NC DIS + CC DIS) events at the Detector Level, as given by the DIS Monte Carlos. $\mathcal{L}$ represents the total luminosity of the sample and A_i is the bin correction factor, defined by equation 5.4

$$A_i = \frac{N_{i,Sig}^{Det}}{N_{i,Sig}^{Had}} \tag{5.4}$$

where $N_{i,Sig}^{Det}$ and $N_{i,Sig}^{Had}$ represent the number of signal (photoproduction) events as given by the photoproduction Monte Carlos at the Detector and Hadron Levels respectively. Due to the limited statistics in the 3-jet sample, large statistical errors result in the trigger efficiency study. To combat this problem, for 3-jet cross sections the trigger efficiency for the appropriate P_T^{jet1} bin is taken. For 2-jet cross sections, the trigger efficiency of the bin into which the event falls is used.

5.7.1 Purity, Stability and Correction Factors

In order to study the migrations between Detector and Hadron Level bins, the bin purities, P_i and stabilities, S_i, defined in equations 5.5 and 5.6, are considered.

$$P_i = \frac{N_{i,Sig}^{Stay}}{N_{i,Sig}^{Det}} \tag{5.5}$$

$$S_i = \frac{N_{i,Sig}^{Stay}}{N_{i,Sig}^{Had*}} \tag{5.6}$$

N_{Sig}^{Stay} represents the number of signal events that fall into the same bin at the Detector and Hadron Levels. $N_{i,Sig}^{Had*}$ denotes the number of signal events in the i^{th} Hadron Level bin that also pass the Detector Level cuts.

The bin purity is sensitive to the fraction of events that migrate into the Detector Level bin. The bin stability considers the fraction of events migrating out of the Hadron Level bin. By construction, the bin stability is insensitive to events that

Purity	Upper Value	Lower Value	Mean
PYTHIA	0.64	0.37	0.48
HERWIG	0.63	0.35	0.48

Table 5.2: *The upper, lower and average values of the purities for PYTHIA and HERWIG.*

Stability	Upper Value	Lower Value	Mean
PYTHIA	0.94	0.56	0.81
HERWIG	0.94	0.70	0.82

Table 5.3: *The upper, lower and average values of the stabilities for PYTHIA and HERWIG.*

pass the Hadron Level cuts but fail the Detector Level cuts. This effect is studied separately by considering the correction factors of each bin.

Figures 5.15, 5.16 and 5.17 show the purities, stabilities and correction factors respectively for the P_T^{jet1} and M^{123} cross sections. The upper, lower and average values of the distributions, calculated from all measured bins, are given for PYTHIA and HERWIG in tables 5.2, 5.3 and 5.4.

Correction Factor	Upper Value	Lower Value	Mean
PYTHIA	1.39	0.88	1.04
HERWIG	1.6	0.94	1.15

Table 5.4: *The upper, lower and average values of the correction factors for PYTHIA and HERWIG.*

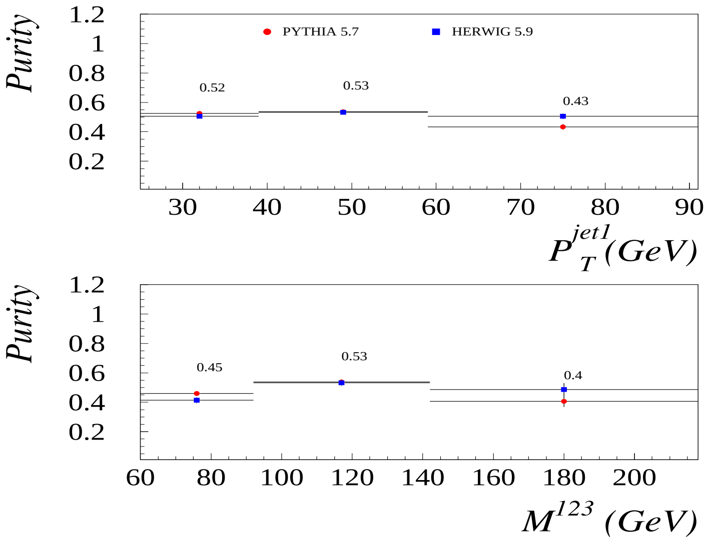

Figure 5.15: *The bin purities for P_T^{jet1} and M^{123} cross sections as given by PYTHIA and HERWIG. The numerical values are for PYTHIA.*

The good agreement between Monte Carlo and data distributions at the Detector Level gives confidence that the migrations in the data are well understood. The correction factors as given by PYTHIA are used to correct the data.

5.8 Error Analysis

In addition to the statistical errors, which are assumed to follow a Poisson distribution, a number of systematic errors are considered.

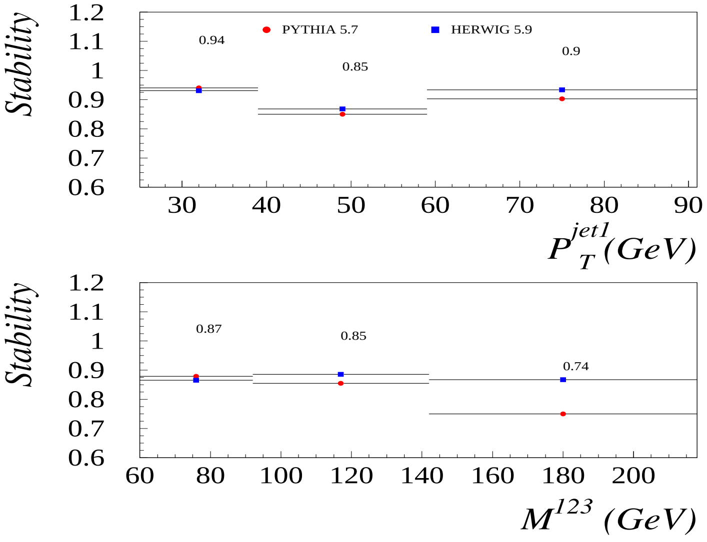

Figure 5.16: *The bin stabilities for P_T^{jet1} and M^{123} cross sections as given by PYTHIA and HERWIG. The numerical values are for PYTHIA.*

5.8.1 Hadronic Energy Scale

Dedicated studies have determined the absolute hadronic energy scale to a precision of better than ±4% [13]. Varying the energies of HFS objects by this amount has a significant effect (∼16%) on each bin and is the dominant systematic error in this measurement.

5.8.2 Acceptance Correction

An uncertainty arises in correcting for detector effects if the distributions at the Detector Level in data and Monte Carlo do not exactly match. Since both PYTHIA

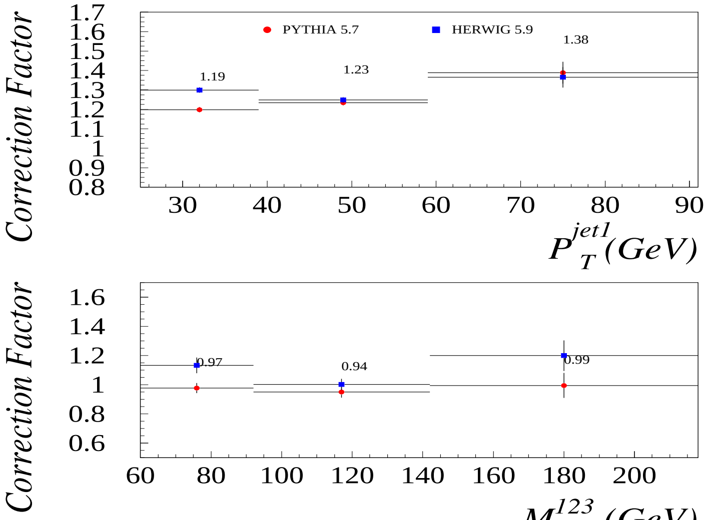

Figure 5.17: *The correction factors for P_T^{jet1} and M^{123} cross sections as given by PYTHIA and HERWIG. The numerical values are for PYTHIA.*

and HERWIG give good agreement in shape with the data distributions, the absolute difference between the correction factors obtained using the two Monte Carlos is used to estimate this uncertainty, which is found to be typically at the 10% level.

5.8.3 Trigger Efficiency

Uncertainties may arise in the trigger efficiency study due to the lack of an independent monitor subtrigger which still fires for events kept with all cuts applied (see Section 5.2.3). For the 2-jet sample, the uncertainty is estimated to be half the inefficiency of the bin plus an additional 3%. Half the inefficiency of the least efficient

P_T^{jet1} bin plus 3% is used for the 3-jet sample. This reflects the increased uncertainty caused by using the P_T^{jet1} trigger efficiency (see Section 5.7) for the 3-jet cross sections. The average uncertainty associated with the trigger efficiency calculation is estimated to be 3.5%.

5.8.4 Luminosity

A luminosity uncertainty of 1.5% is used, corresponding to the precision of the luminosity measurement.

5.8.5 SpaCal Energy Scale

The BEMC and SpaCal energy scales are both known to an accuracy of 7%. Varying the energies of HFS objects in the BEMC and SpaCal by this amount has a negligible effect ($\sim 0.3\%$) on the cross sections.

5.8.6 NC DIS Monte Carlo Normalisation

RAPGAP overestimates the 2-jet and 3-jet production rate in NC DIS at low Q^2. The uncertainty arising from this is conservatively estimated by varying the NC DIS cross section by a factor of two. Since greater than 96% rejection of NC DIS events is achieved in all measured bins by the anti-NC DIS cuts of Section 5.4.2, this has only a small effect on all cross sections ($\sim 0.9\%$).

Chapter 6

Discussion of Results

In this chapter, the Hadron Level *ep* cross sections measured using the analysis chain described in Chapter 5 are presented. After considering the structure of the 2-jet and 3-jet cross-sections the predictions, given by the event generators PYTHIA and HERWIG and the numerical integration program JetViP, are compared to the data. All the data points have been passed by the H1 Collaboration as Preliminary results, as have the PYTHIA comparisons [68]. Preliminary comparisons show that the results agree well with data in the same kinematic region from the ZEUS collaboration [45, 69].

6.1 Hadron Level Cross Sections

6.1.1 2-jet Cross Sections

In figures 6.1 and 6.2 the Hadron Level *ep* 2-jet cross sections as a function of leading jet transverse momentum, P_T^{jet1} between $25 < P_T^{jet1} < 91$ GeV and average transverse momentum of the top two jets, $\overline{P_T^{12}}$ between $20 < \overline{P_T^{12}} < 91$ GeV respectively are shown. The cross sections fall by three orders of magnitude in the measured ranges.

The Hadron Level *ep* 2-jet cross section as a function of the invariant mass of the top two jets, M^{12} is shown in figure 6.3 over the range $43 < M^{12} < 180$ GeV . The cross section falls by over three orders of magnitude. In these figures, the predictions of PYTHIA and HERWIG and the Parton Level cross sections at LO and NLO as implemented in the JetViP program are shown.

6.1.2 3-jet Cross Sections

The Hadron Level *ep* 3-jet cross section as a function of third jet transverse momentum, P_T^{jet3} , over the range $10 < P_T^{jet3} < 51$ GeV , is shown in figure 6.4. The Hadron Level *ep* 3-jet cross sections as a function of the invariant mass of the top two jets, M^{12} , in the range $43 < M^{12} < 180$ GeV , the first and third jet, M^{13} , in the range $45 < M^{13} < 138$ GeV and the second and third jet, M^{23} , in the range $30 < M^{23} < 100$ GeV are shown in figures 6.5, 6.6 and 6.7 respectively. Finally, the Hadron Level *ep* 3-jet cross section as a function of the invariant mass of the top three jets, M^{123} in the range $60 < M^{123} < 218$ GeV is shown in figure 6.8. As with the 2-jet cross sections the 3-jet cross sections fall by up to three orders of magnitude over the ranges. The predictions of PYTHIA and HERWIG and the Parton Level cross sections at LO and NLO as implemented in the JetViP program are again shown for comparison.

6.2 JetViP Comparison

Since JetViP does not include a hadronisation scheme, the cross sections produced are at the Parton Level. In order to study the effects of hadronisation on the partonic

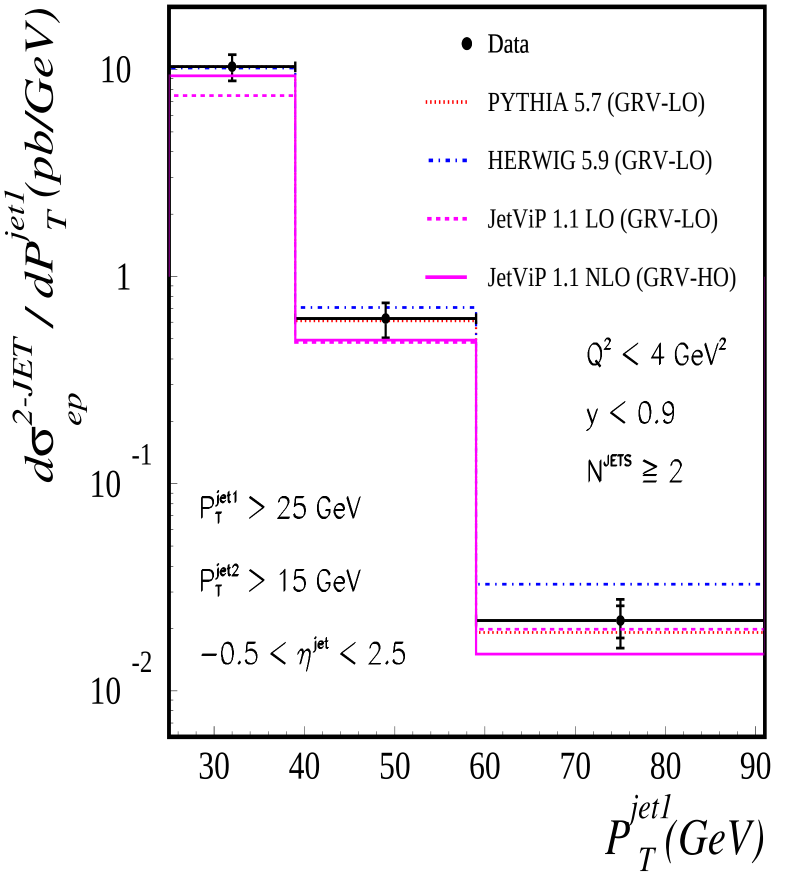

Figure 6.1: *Hadronic ep cross section for 2-jet production as a function of the transverse momentum of the leading jet,* P_T^{jet1} *. The inner error bars denotes the statistical, the outer error bars the quadratic sum of all statistical and systematic errors of the data. The predictions given by the PYTHIA 5.7 and HERWIG 5.9 programs, using GRV LO structure functions for the proton and photon are shown, as are the LO and NLO parton cross sections implemented with the JetViP 1.1 numerical integration program using GRV LO and HO structure functions respectively. The HERWIG and PYTHIA cross sections have been scaled to the data cross section.*

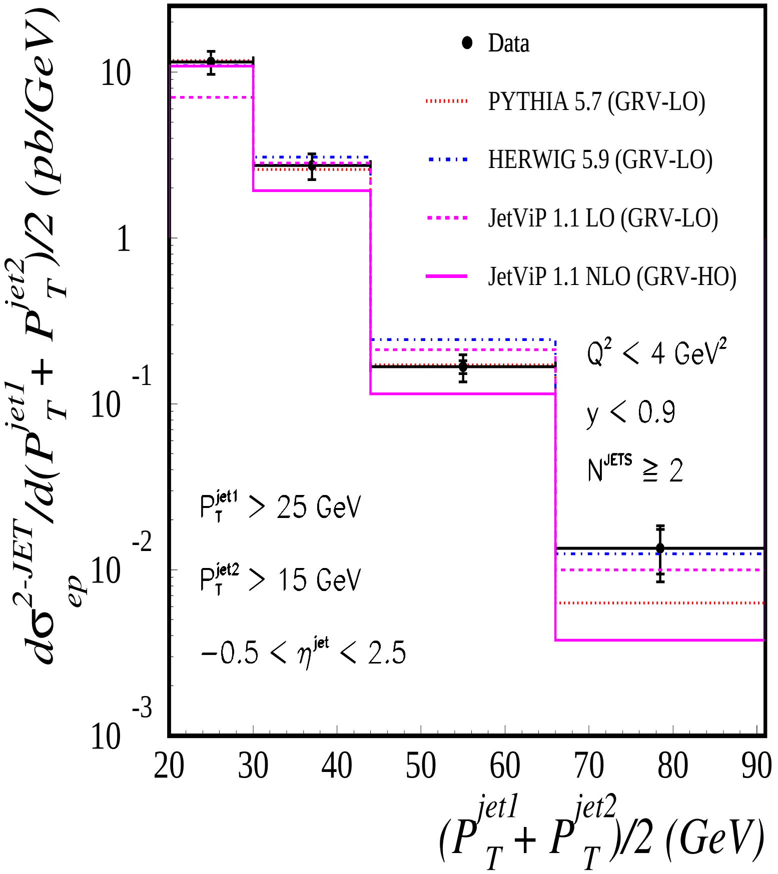

Figure 6.2: *Hadronic ep cross section for 2-jet production as a function of the average transverse momentum of the two leading jets,* P_T^{jet1} *and* P_T^{jet2} *. The inner error bars denotes the statistical, the outer error bars the quadratic sum of all statistical and systematic errors of the data. The predictions given by the PYTHIA 5.7 and HERWIG 5.9 programs, using GRV LO structure functions for the proton and photon are shown, as are the LO and NLO parton cross sections implemented with the JetViP 1.1 numerical integration program using GRV LO and HO structure functions respectively. The HERWIG and PYTHIA cross sections have been scaled to the data cross section.*

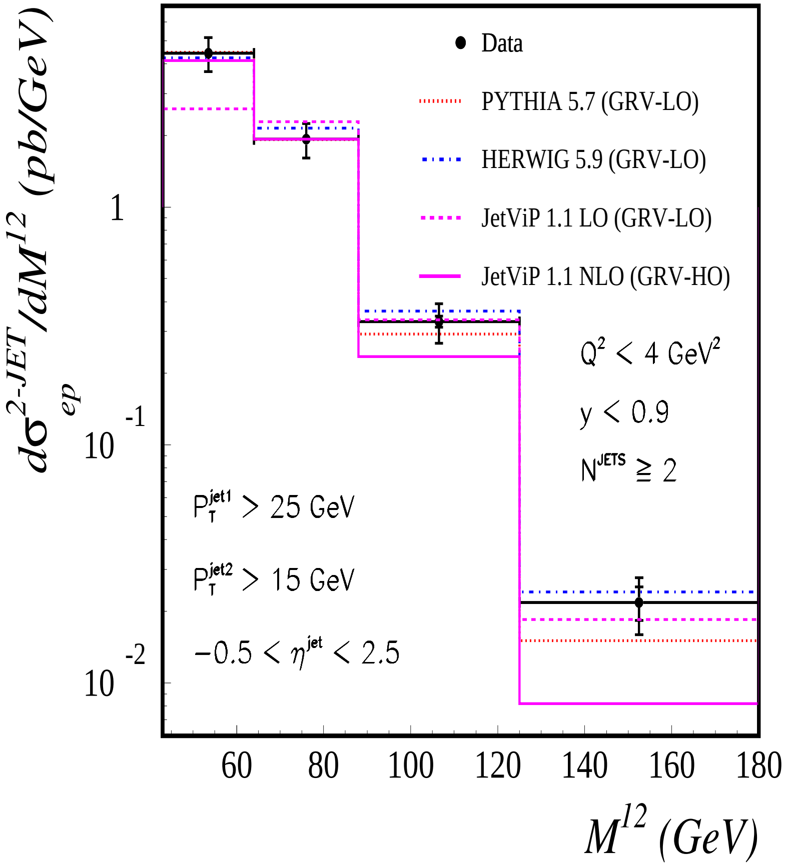

Figure 6.3: *Hadronic ep cross section for 2-jet production as a function of the invariant mass of the two leading jets,* M^{12} *. The inner error bars denotes the statistical, the outer error bars the quadratic sum of all statistical and systematic errors of the data. The predictions given by the PYTHIA 5.7 and HERWIG 5.9 programs, using GRV LO structure functions for the proton and photon are shown, as are the LO and NLO parton cross sections implemented with the JetViP 1.1 numerical integration program using GRV LO and HO structure functions respectively. The HERWIG and PYTHIA cross sections have been scaled to the data cross section.*

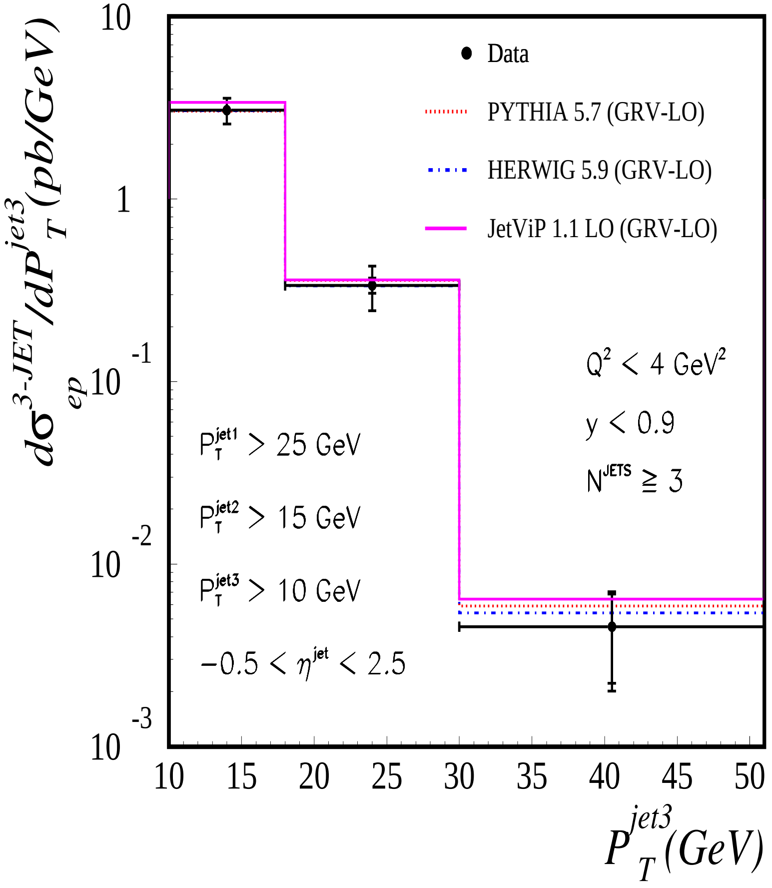

Figure 6.4: *Hadronic ep cross section for 3-jet production as a function of the transverse momentum of the third jet,* P_T^{jet3} *. The inner error bars denotes the statistical, the outer error bars the quadratic sum of all statistical and systematic errors of the data. The predictions given by the PYTHIA 5.7 and HERWIG 5.9 programs, using GRV LO structure functions for the proton and photon are shown, as is the LO parton cross sections implemented with the JetViP 1.1 numerical integration program using GRV LO structure functions. The HERWIG and PYTHIA cross sections have been scaled to the data cross section.*

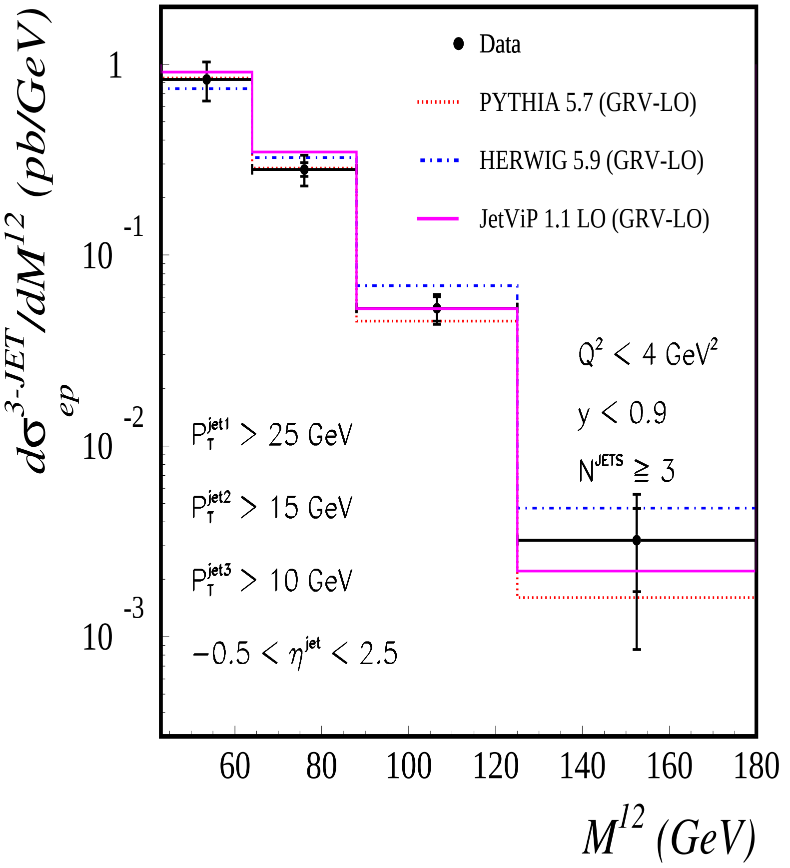

Figure 6.5: *Hadronic ep cross section for 3-jet production as a function of the invariant mass of the two leading jets,* M^{12} *. The inner error bars denotes the statistical, the outer error bars the quadratic sum of all statistical and systematic errors of the data. The predictions given by the PYTHIA 5.7 and HERWIG 5.9 programs, using GRV LO structure functions for the proton and photon are shown, as is the LO parton cross sections implemented with the JetViP 1.1 numerical integration program using GRV LO structure functions. The HERWIG and PYTHIA cross sections have been scaled to the data cross section.*

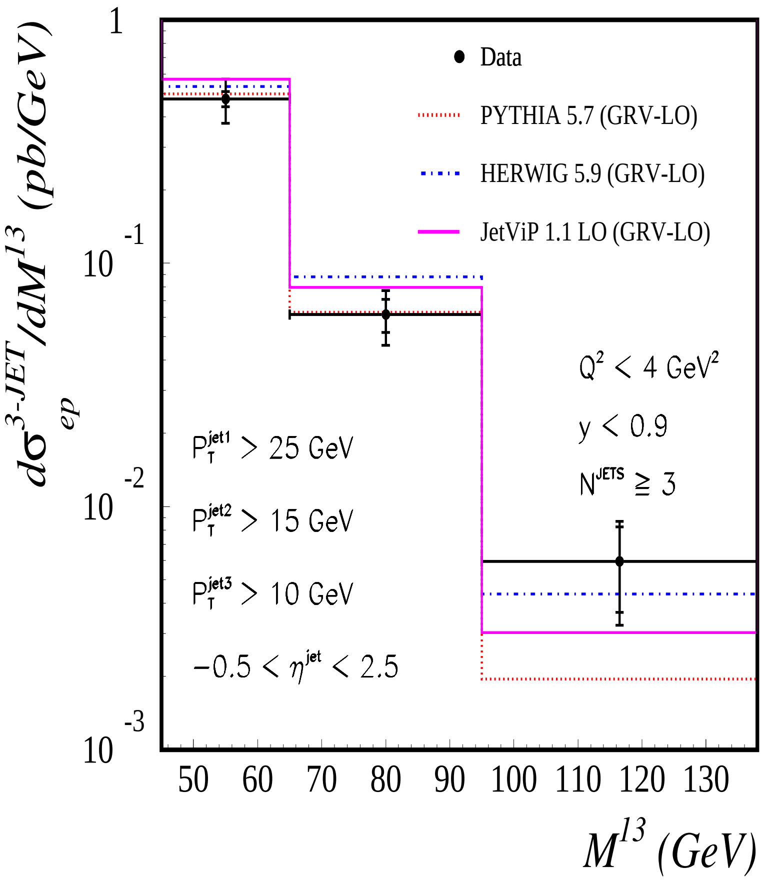

Figure 6.6: *Hadronic ep cross section for 3-jet production as a function of the invariant mass of the first and third jets, M^{13} . The inner error bars denotes the statistical, the outer error bars the quadratic sum of all statistical and systematic errors of the data. The predictions given by the PYTHIA 5.7 and HERWIG 5.9 programs, using GRV LO structure functions for the proton and photon are shown, as is the LO parton cross sections implemented with the JetViP 1.1 numerical integration program using GRV LO structure functions. The HERWIG and PYTHIA cross sections have been scaled to the data cross section.*

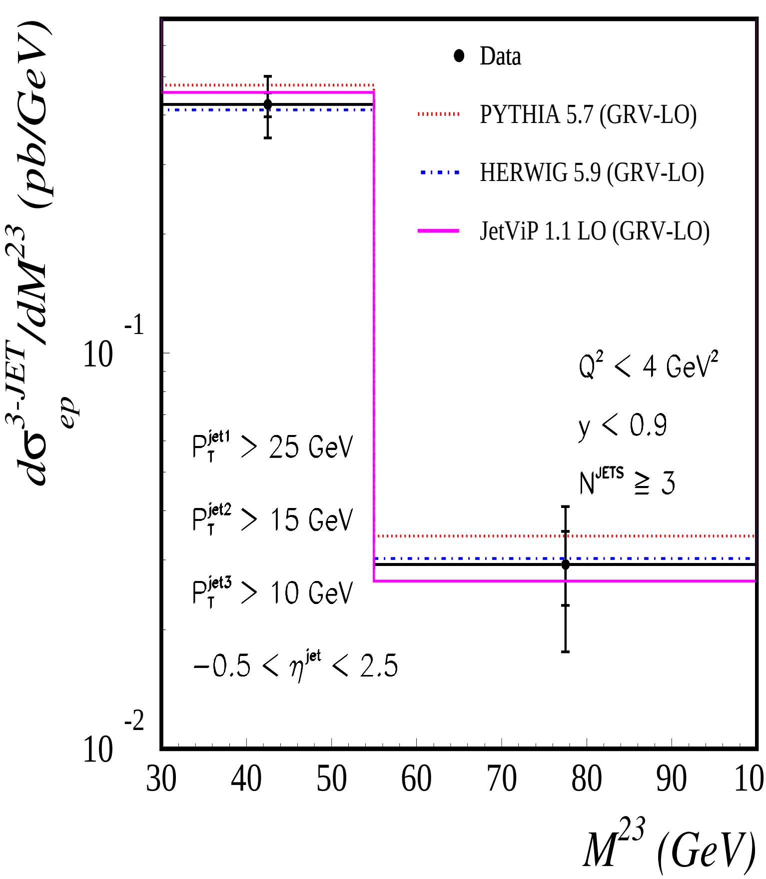

Figure 6.7: *Hadronic ep cross section for 3-jet production as a function of the invariant mass of the second and third jets, M^{23} . The inner error bars denotes the statistical, the outer error bars the quadratic sum of all statistical and systematic errors of the data. The predictions given by the PYTHIA 5.7 and HERWIG 5.9 programs, using GRV LO structure functions for the proton and photon are shown, as is the LO parton cross sections implemented with the JetViP 1.1 numerical integration program using GRV LO structure functions. The HERWIG and PYTHIA cross sections have been scaled to the data cross section.*

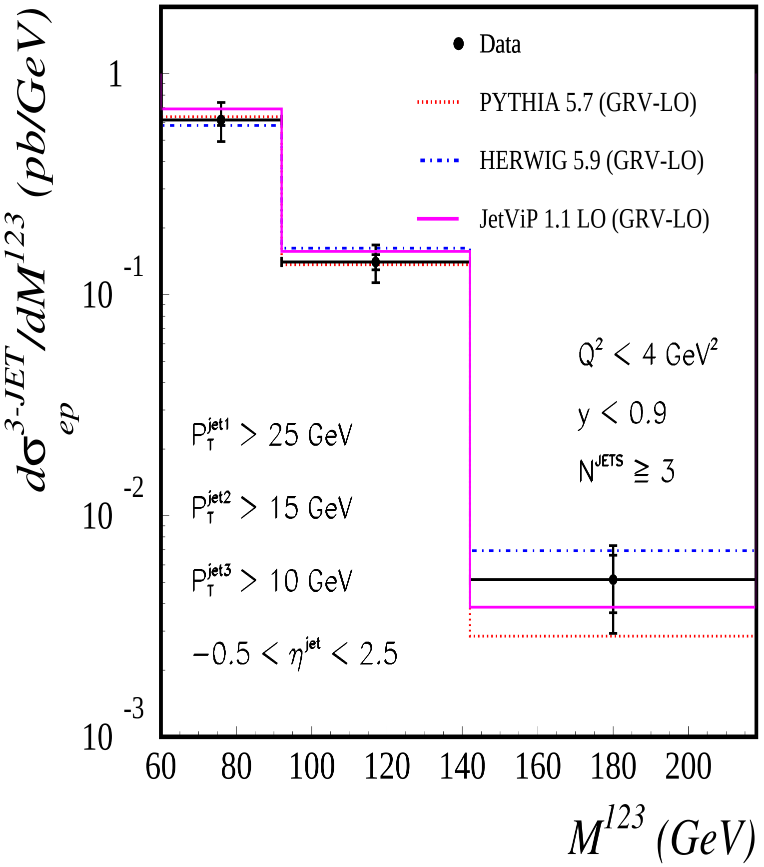

Figure 6.8: *Hadronic ep cross section for 3-jet production as a function of the invariant mass of the three leading jets, M^{123} . The inner error bars denotes the statistical, the outer error bars the quadratic sum of all statistical and systematic errors of the data. The predictions given by the PYTHIA 5.7 and HERWIG 5.9 programs, using GRV LO structure functions for the proton and photon are shown, as is the LO parton cross sections implemented with the JetViP 1.1 numerical integration program using GRV LO structure functions. The HERWIG and PYTHIA cross sections have been scaled to the data cross section.*

H_i^c	Upper Value	Lower Value	Mean
PYTHIA	1.32	0.95	1.11
HERWIG	1.18	0.86	1.01

Table 6.1: *The upper, lower and average values of the hadronisation corrections in all measured cross section bins for PYTHIA and HERWIG.*

cross sections, the PYTHIA and HERWIG predictions, before and after the outgoing partons have been hadronised, are considered. Since the two Monte Carlo programs implement different hadronisation schemes (see Section 4.6), an estimate of the likely effect of hadronisation on Partonic cross sections, without being dependent on a single model, is gained. The hadronisation correction, H_i^c , is defined below

$$H_i^c = \frac{\sigma_i^{Had}}{\sigma_i^{Part}} \qquad (6.1)$$

where σ_i^{Had} and σ_i^{Part} are the cross sections in the i^{th} bin at the Hadron and Parton Level respectively. The upper, lower and average values of H_i^c for all measured bins as given by PYTHIA and HERWIG are shown in table 6.1.

Given their small impact, it is considered preferable not to apply the hadronisation corrections to the Parton Level cross sections, since this would introduce an unwanted model dependency.

Both the LO and, for the 2-jet cross sections, the NLO JetViP predictions agree well with the data in most bins. However, for the 2-jet cross sections, the asymmetric jet cuts allow a region of phase space ($P_T^{jet2} < P_T^{jet1} \sim 25$ GeV) to be populated by the NLO predictions and the data which is not possible for the LO predictions. Therefore, the first bin of each 2-jet cross section is always underestimated by the LO prediction. The slope of the LO 2-jet predictions is less steep than that of the NLO, showing that the inclusion of higher order terms in the QCD calculation significantly affects the predicted cross section. The steeper NLO slope is consistent with the presence of a hard third jet in the NLO case, reducing the likelihood of high P_T and high mass states being formed by the top two jets.

6.3 Monte Carlo Comparison

6.3.1 QCD Event Generators

Both PYTHIA and HERWIG agree well with the data, after the scale factors in table 5.1 have been applied. The slope of the HERWIG cross sections tend to be less steep than in PYTHIA. The differences in slope and overall normalisation can both explained by the different treatment of α_s in the two Monte Carlos. This also explains the difference in the jet multiplicity spectrum, shown in figure 5.9.

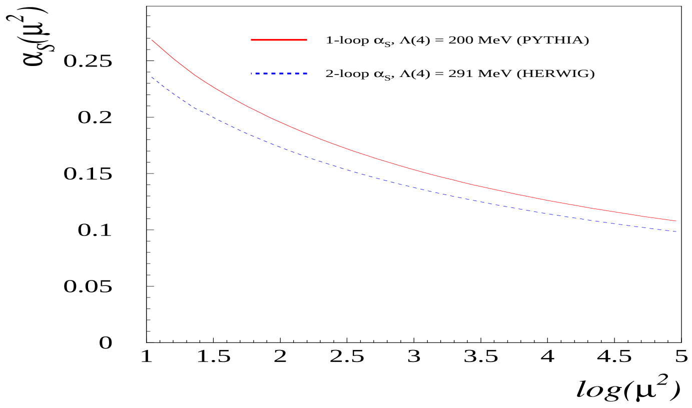

Figure 6.9: *1-loop and 2-loop* α_s *as a function of scale,* μ *showing the different values of the couplings used in PYTHIA and HERWIG.*

The same evolution with scale, μ (see figure 6.9) governs the α_s used in the matrix elements and the parton showering of each Monte Carlo (1-loop for PYTHIA, 2-loop for HERWIG). Since the HERWIG α_s is lower than PYTHIA's, the probability of a third hard parton being produced is less in a HERWIG interaction than in PYTHIA. Consequently, the jet multiplicity spectrum in HERWIG shows a higher 2-jet : 3-jet ratio than does PYTHIA and the HERWIG cross sections fall less steeply. The overall normalisation will also be reduced in HERWIG with respect to PYTHIA, since cross sections may be pictured as an expansion series in α_s . Varying the factorisation scale of the $PDF's$ alters the cross sections by $\sim 30\%$. This would explain the difference in normalisation between PYTHIA and the data.

Although PYTHIA and HERWIG implement different hadronisation schemes, the differences in the jet multiplicity spectrum persist at the Parton Level. It is therefore unlikely that the use of separate hadronisation models is the cause of the differences in the jet multiplicity distributions at the Detector Level. Since the differing α_s values used can explain all the differences between PYTHIA and HERWIG and the hadronisation corrections are known to be small from table 6.1, there is no evidence to suggest that the difference in hadronisation models causes the difference in the Hadron Level cross section predictions made by PYTHIA and HERWIG.

In summary, the QCD predictions (JetViP, PYTHIA and HERWIG) are able to describe the shape of all the measured cross sections. Therefore, no additional contributions from heavy particle decay are required.

6.3.2 W Production

Using the EPVEC generator, the Hadron Level ep cross sections for W production were investigated. In all measured bins, the cross section was less than 10% of the PYTHIA cross section, with the average being $\approx 2\%$. This agrees with the observation that the measured cross sections can be described by the QCD predictions. The bin with the highest proportion of EPVEC to PYTHIA events was the highest mass bin of the M^{123} distribution, in which $\approx 8\%$ of the cross section could be attributed to W production. Given the low proportion of W to 'QCD background' events, and the lack of statistics in the high mass bins, no attempt has been made to extract a W production cross section from the data.

Chapter 7

Summary

The dominant component of the total ep cross section at HERA comes from the interaction of protons with almost on-shell photons; the photoproduction regime. The large γp centre-of-mass energy allows hard interactions to take place and a clear jet structure is visible in these events. By measuring 2-jet and 3-jet cross sections in the limit of high jet transverse momentum and invariant mass of multijet systems, the validity of QCD can be tested in hitherto unexplored kinematic regions. These cross sections are also sensitive to the hadronic decays of a high mass particle, such as those suggested to explain the excess of isolated events recently observed by the H1 collaboration. The Longitudinally Invariant K_T algorithm has been used to define the jets and the kinematic range of the measurement is restricted to Q^2 < 4 GeV^2 and $y < 0.9$. The cross sections fall by three orders of magnitude in the measured range.

The predictions of the QCD-inspired event generators PYTHIA 5.7 and HERWIG 5.9 (using GRV LO structure functions) agree well in shape with the data but require an overall scale factor to be applied which differs for the 2-jet and 3-jet cases. The HERWIG scale factors are considerably larger than those for PYTHIA. The different treatments of the strong coupling constant, α_s is assumed to be the cause of the difference and also explains the slightly steeper cross section slope observed in the PYTHIA predictions. The factorisation scale uncertainty is sufficient to cause a normalisation difference of $\sim 30\%$ between the data and Monte Carlo predictions.

The numerical integration program JetViP 1.1 includes all relevant $\mathcal{O}(\alpha_s^2)$ and $\mathcal{O}(\alpha_s^3)$ matrix elements (unlike PYTHIA and HERWIG). For the 2-jet cross sections, the NLO corrections can therefore be studied. The JetViP predictions agree well with the data in shape and normalisation except close to the asymmetric P_T^{jet} cut, where the LO 2-jet cross section prediction fails, as expected from tranvserse momentum conservation. The difference in slope between the $\mathcal{O}(\alpha_s^2)$ and $\mathcal{O}(\alpha_s^3)$ JetViP predictions for the 2-jet cross sections is consistent with the emission of a third hard jet in the NLO case and shows the importance of higher order terms in the QCD calculation.

7.1 Outlook for the Future

The future for high P_T^{jet} measurements in photoproduction looks bright. For the first time at H1, the QCD contribution to the high P_T^{jet} cross sections has been determined, paving the way for more exclusive analyses into heavy particle decay. These will be aided by the increased luminosity already available from the 1998 and 1999 data taking periods, and the significantly higher luminosities that can be expected following the luminosity upgrade program, scheduled for 2001.

Appendix A

Comparing Cone and Cluster Algorithms

Since an algorithm-independent jet definition is not possible, it is useful to quantify the differences between jet algorithms. To this end, the results of implementing the thesis analysis chain with three separate jet algorithms is presented. The algorithms chosen are those most often used in recent jet publications - the Longitudinally Invariant K_T Algorithm (a clustering algorithm and the default for this thesis) and the PXCONE algorithm with two cone radii; R=1 and R=0.7.

For the 2-jet cross sections (figures A.1 *a*) and *c*)), the PXCONE algorithm with radius, R=1 and the K_T algorithm give similar results, while the R=0.7 PXCONE mode lies below the other two. For the 3-jet sample (figures A.1 *b*) and *d*)), the R=1 cross section lies below the K_T cross section, with the R=0.7 cross section remaining below both.

Jets in the same event, reconstructed using an R=1 cone will tend to have a higher P_T^{jet} than jets reconstructed using an R=0.7 cone for the following two reasons:

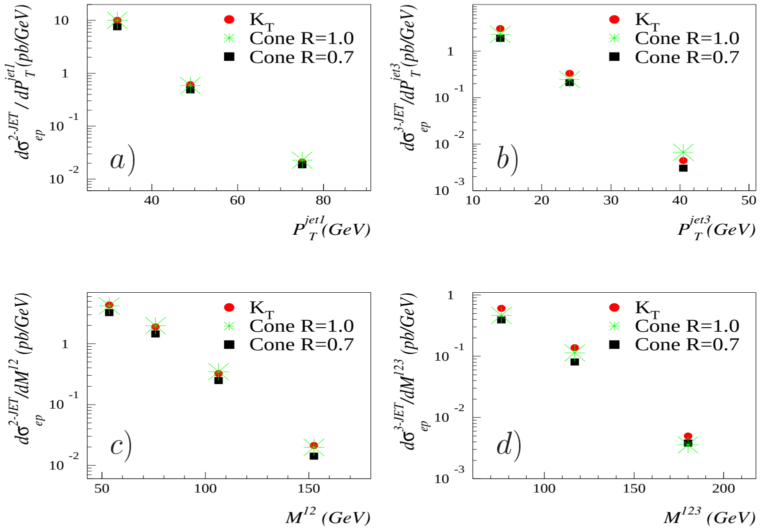

Figure A.1: *The Hadron Level cross sections for a) the leading jet P_T , b) the third jet P_T , c) the 2-jet invariant mass of the highest two P_T jets and d) the 3-jet invariant mass of the highest three P_T jets. The superscripts '$2-JET$' and '$3-JET$' are used for cross sections where two and three jets are required respectively. Error bars are not shown.*

- Multiple interactions (see section 4.7.1) between the proton and photon remnants produce low energy particles which form a 'pedestal' upon which the hadrons from the hard scatter sit. The larger the cone radius of the algorithm, the more P_T from the pedestal is picked up.

- If the width of a group of hadrons originating from the hard scatter exceeds the radius of the algorithm, those hadrons falling outside the jet cone will not contribute to the jet P_T . Again the larger the cone radius, the higher the

resulting P_T^{jet} .

Since all the measured cross sections fall steeply with increasing P_T^{jet} , the R=1 algorithm therefore gives a higher cross section than the R=0.7 algorithm.

That neither cone algorithm matches the K_T algorithm for both 2-jet and 3-jet cross sections highlights the fact that K_T and cone algorithms form jets in fundamentally different ways. The K_T algorithm can be said to concentrate on the core of the jet whilst cone algorithms seek to maximise the jet energy and so pull in as much neighbouring energy as possible [43]. Therefore, cone algorithms will tend to suppress the reconstruction of a third jet close to either of the two leading jets. This leads to a reduction in the 3-jet cross section for cone algorithms with respect to K_T , as is seen in figure A.1. The good agreement between the R=1 cone and the K_T 2-jet cross-sections is also observed in [72].

Appendix B

The Need for Asymmetric Jet Cuts

In [73], the behaviour of the inclusive 2-jet cross section, σ_2 in photoproduction at next-to-leading order is studied as a function of Δ, where

$$\sigma_2(\Delta) = \sigma(E_{1T} > E_T^{cut}, E_{2T} > E_T^{cut} + \Delta). \tag{B.1}$$

The authors use an alternative nomenclature to that adopted in this thesis. The highest transverse energy jet is labelled '2' and the second highest as '1' so that the first and second highest transverse energy jets are labelled E_{2T} and E_{1T} respectively. The kinematic region is restricted to $Q^2 < 4$ GeV^2, $y = 0.8$ (equivalent to $W_{\gamma p} = 268$ GeV). Their results are shown in figure B.1.

As Δ tends to zero, the NLO cross section does not rise monotonically. This behaviour is caused by a dependence on an infra-red cutoff parameter, δ, which is introduced to separate the divergent piece of the real corrections from the finite piece. For $\Delta \gg 0$, the dependence on δ of the real NLO corrections is completely

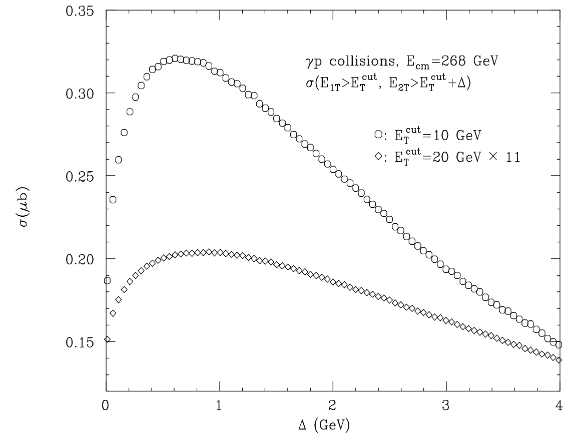

Figure B.1: *The inclusive 2-jet total cross section for* $E_{1T} > E_T^{cut}$ *and* $E_{2T} > E_T^{cut} + \Delta$*, as a function of* Δ*, for two different values of* E_T^{cut}*. The* γp *centre of mass energy is labelled as* E_{cm}*.*

cancelled by an equal and opposite term in the virtual corrections. However, for $\Delta \simeq 0$, real soft gluon emission is suppressed, as the two hardest partons have equal and opposite transverse energies. The momentum of the internal gluon loop in the virtual part of the cross section is unaffected. This suppression of the real δ dependence prevents cancellation of the δ term and an unphysical turn-over of the NLO cross section results. Since the true cross section will not exhibit this behaviour, NLO predictions for $\Delta \approx 0$ can be unreliable. The choice of $\Delta = 10$ GeV is felt to be sufficiently far from the turnover region to avoid the problem.

Bibliography

[1] E.D. Bloom et al., Phys. Rev. Lett. **23** (1969) 930;
M. Breidenbach et al., Phys. Rev. Lett. **23** (1969) 935.

[2] D.J. Fox et al., Phys. Rev. Lett. **33** (1974) 1504;
Y. Watanabe et al., Phys. Rev. Lett. **35** (1975) 898;
H.L. Anderson et al., Phys. Rev. Lett. **38** (1977) 1450;
B.A. Gordon et al., Phys. Rev. Lett. **41** (1978) 615;
EMC Collab., J.J. Aubert et al.,Nucl. Phys. **B213** (1983) 31;
CDHS Collab., H. Abramowicz et al., Z. Phys., **C25** (1984) 29;
BEBC Collab., K. Varvell et al., Z. Phys. **C36** (1987) 1;
CDHSW Collab., P. Berge et al., Z. Phys., **C49** (1991) 187;
CCFR Collab., P.Z. Quintas et al., Phys Rev. Lett. **71** (1993) 1307;
E665 Collab., M.R. Adams et al., Z. Phys **C67** (1995) 403.

[3] BCDMS Collab., A.C. Benvenuti et al., Phys. Lett. **B223** (1989) 485.

[4] NMC Collab., M. Arneodo et al., Phys. Lett. **B364** (1995) 107.

[5] H1 Collab., S. Aid et al., Nucl. Phys. **B470** (1996) 3.

[6] ZEUS Collab., M. Derrick et al., Z. Phys. **C72** (1996) 399.

[7] T. Sjöstrand, CERN-TH-6488 (1992), Comput. Phys. Commun. **82** (1994) 74.

[8] G. Marchesini et al., Comp. Phys. Comm. **67** (1992) 465.

[9] B. Pötter, Comput. Phys. Commun. **119** (1999) 45.

[10] H1 Collaboration; I. Abt et al., Nucl. Instr. and Meth. **A386** (1997) 310-348.

[11] H1 Calorimeter Group; B. Andrieu et al., Nucl. Instr. and Meth. **A336** (1993) 460.

[12] H1 SPACAL group, R.D. Appuhn et al., Nucl. Instr. and Meth. **A386** (1997) 397.

[13] Beate Heinemann; Dissertation : "Measurement of Charged Current and Neutral Current Cross Sections in Positron-Proton Collisions at $\sqrt{s} = 300\ GeV$".

[14] H1 Collaboration; C Adloff et al.,submitted to Eur Phys J C, "Measurement of Neutral and Charged Current Cross-Sections in Positron-Proton Collisions at Large Momentum Transfer".

[15] S. Burke et al., RAL **95-037**. DESY **95-132**.

[16] J. Burger et al., Nucl. Instr. and Meth. **A279** (1989) 217.

[17] S. Egli et al., Nucl. Instr. and Meth. **A283** (1989) 487.

[18] K. Muller et al., Nucl. Instr. and Meth. **A312** (1992) 457.

[19] J. Heatherington et al., Studies on TOF FTDC data. H1 Internal Note **93-307**;
J. Heatherington et al., Analysis of TOF FTDC data. H1 Internal Note **94-362**.

[20] H. Bethe, W. Heitler, Proc. Roy. Soc. **A146** (1934) 83.

[21] E. Elsen, The H1 Trigger and Data Acquisition. Proc. of the International Symposium on Electronic Instrumentation in Physics, Dubna, May 1991. H1 Internal Note **93-262**;
F. Sefkow et al., Experience with the First Level Trigger of H1. Proc. of the

1994 IEEE Nuclear Science Symposium, Norfolk, Virginia. H1 Internal Note **94-407**.

[22] R. Brun et al., GEANT3 User's Guide, CERN-DD/EE-84-1 (1987).

[23] H1 Collab., T. Ahmed et al., Phys. Lett. **B324** (1994) 241;
H1 Collab., S. Aid et al., Z. Phys. **C67** (1995) 565;
H1 Collab., S. Aid et al., Phys. Lett. **B379** (1996) 319.

[24] ZEUS Collab., M. Derrick et al., Phys. Rev. Lett. **75** (1995) 1006;
ZEUS Collab., M. Derrick et al., Z. Phys. **C72** (1996) 47.

[25] H1 Collab., I. Abt et al., Nucl. Phys. **B407** (1993) 515;
H1 Collab., T. Ahmed et al., Nucl. Phys. **B439** (1995) 471.

[26] ZEUS Collab., M. Derrick et al., Phys. Lett. **B316** (1993) 412;
ZEUS Collab., M. Derrick et al., Z. Phys. **C65** (1995) 379.

[27] H1 Collab., S. Aid et al., Z. Phys. **C69** (1995) 27.

[28] ZEUS Collab., M.Derrick et al., Z.Phys. **C63** (1994) 391.

[29] Particle Data Group, L.Montanet et al., Phys. Rev. **D50** (1994) 1173.

[30] A.Donnachie and P.V.Landshoff, Phys. Lett. **B296** (1992) 227.

[31] H.Abramovich, E.M.Levin, A.Levy and U.Maor, Phys. Lett. **B269** (1991) 465.

[32] CDF Collab., F.Abe et al., Phys.Rev. **D50** (1994) 5550.

[33] J.M. Butterworth (for the H1 and ZEUS Collaborations), presented at the Ringberg Workshop, Tegernsee, 25-30 May, 1997.

[34] Armen Bouniatian; Dissertation : "Studies of Hard Scattering in Photoproduction at the *ep* Storage Ring HERA with the H1 Detector".

[35] ZEUS Collab., M. Derrick et al, Phys. Lett. **B384** (1996) 401.

[36] J.R. Forshaw, presented at the 5th International Workshop on Deep Inelastic Scattering and QCD (DIS 97), Chicago, IL, 14-18 Apr 1997.

[37] ZEUS Collab., M. Derrick et al. Phys. Lett. **B348** (1995) 665.

[38] O. Kaufmann, Workshop on new results from HERA, Ringberg Castle 1999 and PhD Thesis, Heidelberg 1998.

[39] H1 Collaboration, C. Adloff et al., DESY 98-148 (1998).

[40] M. Glück, E. Reya and A. Vogt, Phys. Rev. **D46** (1992) 1973

[41] H. Abramowicz, K. Charchula and A. Levy, Phys. Lett. **B269** (1991) 458

[42] PLUTO Collab., Ch. Berger et al., Phys. Lett. **B142** (1984) 111;
PLUTO Collab., Ch. Berger et al., Nucl. Phys. **B281** (1987) 365;
PLUTO Collab., Ch. Berger et al., Phys. Lett. **B107** (1981) 168;
JADE Collab., W. Bartel et al., Z. Phys. **C24** (1984) 231;
TASSO Collab., M. Althoff et al., Z. Phys. **C24** (1984) 231;
TPC/2γ Collab., H. Aihara et al., Phys. Rev. Lett. **58** (1987) 97;
TPC/2γ Collab., H. Aihara et al., Z. Phys. **C34** (1987) 1;
AMY Collab., T. Sasaki et al., Phys. Lett. **B252** (1990) 491;
OPAL Collab., R. Akers et al., Z. Phys. **C61** (1994) 199;
AMY Collab., 2B. J. Kim et al., Phys. Lett. **B325** (1994) 248;
TOPAZ Collab., H. Hayashii et al., Phys. Lett. **B314** (1993) 149;
ALEPH Collab., D. Buskulic et al., Phys. Lett. **B313** (1993) 509;
DELPHI Collab., P. Abreu et al., Phys. Lett. **B342** (1995) 402.

[43] M.H. Seymour, presented at 10th Topical Workshop on Proton-Antiproton Collider Physics, Batavia, IL, 9-13 May 1995.

[44] G. Sterman and S. Weinberg, Phys. Rev. Lett. **39** (1977) 1436.

[45] ZEUS Collab., J. Breitweg et al., Eur. Phys. J. **C11** (1999) 35.

[46] H1 Collab., C. Adloff et al., Nucl. Phys. **B545** (1999) 3.

[47] M.H. Seymour, in: Les Rencontres de la Vallée d'Aoste, La Thuile, France (1997) and Nucl. Phys. **B513** (1998) 269.

[48] L.A. del Pozo, PhD Thesis University of Cambridge, Cambridge, England (1993) RALT-002.

[49] CDF Collab., F. Abe et al., Phys. Rev. **D45** (1992) 1448.

[50] OPAL Collab., R. Akers et al., Z. Phys. **C63** (1994) 197 and Z. Phys. C 68 (1995) 179.

[51] Jade Collab., S. Bethke et al., Phys. Lett. **B213** (1988) 235.

[52] S.D. Ellis and D.E. Soper, Phys. Rev. **D48** (1993) 3160.

[53] S. Catani, Yu.L. Dokshitzer, M.H. Seymour and B.R. Webber, Nucl. Phys. **B406** (1993) 187.

[54] H. Baer, J. Ohnemus and D. Zeppenfeld, Z. Phys. **C43**, 675 (1989).

[55] T. Sjöstrand, M. Bengtsson, Comp. Phys. Comm. **43** (1987) 367.

[56] H1 Collab., S. Aid et al., Z. Phys. **C70** (1996) 17.

[57] H1 Collab., C. Adloff et al., Eur. Phys. J. **C1** (1998) 97.

[58] J.M. Butterworth, J.R. Forshaw and M.H. Seymour, Z. Phys. **C72** (1996) 637.

[59] B. Cox, J. Forshaw and L. Lönnblad, JHEP **10**, 023 (1999).

[60] U. Baur, J.A.M. Vermaseren and D. Zeppenfeld, Nucl. Phys. **B375** (1992) 3.

[61] A. Kwiatkowski, H. Spiesberger and H.-J. Möhring, Comp. Phys. Comm. **69** (1992) 155.

[62] H. Jung, Comp. Phys. Comm. **86** (1995) 147.

[63] G. A. Schuler and H. Spiesberger, Proceedings of the Workshop "Physics at HERA", vol. 3, eds. W. Buchmüller, G. Ingelman, DESY (1992) 1419.

[64] L. Lönnblad, Comp. Phys. Comm. **71** (1992) 15.

[65] G.P. Lepage, J. Comp. Phys. **27** (1978) 192.

[66] H1 Collab., C. Adloff et al.; Eur. Phys. J. **C5**, 575 (1998).

[67] H. Fritzsch and D. Holtmannspotter, Phys. Lett. **B457** (1999) 186.

[68] H1 Collab., "Test of the Standard Model in high P_T jet production at HERA", procedings of the International Conference on High Energy Physics, HEP99, Tampere, Finalnd, July 1999.

[69] ZEUS Collab., J. Breitweg et al., Phys. Lett. **B443** (1998) 394.

[70] L.E. Gordon and J.K. Storrow, Z. Phys. **C56** (1992) 307.

[71] P. Aurenche, M. Fontannez, J.Ph. Guillet, Z. Phys. **C64** (1994) 621.

[72] ZEUS Collab., C. Glasman, presented at the International Europhysics Conference on High-Energy Physics (EPS-HEP 99), Tampere, Finland, July 1999.

[73] S. Frixione and G. Ridolfi, Nucl. Phys. **B507** (1997) 315.

Acknowledgements

This thesis would not have been possible without the contributions and support of many people. Firstly, I wish to thank my supervisor Robin Marshall. From the start, he has encouraged me to find an analysis which I would enjoy and has given support and guidance whenever I needed it. Special thanks must also go to Andrew Mehta for his ideas and inspiration. I would also like to thank Jeff Forshaw, Mike Seymour, Björn Pötter and Markus Wobisch for their clear and understandable explanations of the complexities of QCD and jet physics. Also, Fred Loebinger for making me choose Manchester University as an undergraduate and postgraduate, choices I have never looked back on. Mike Ibbotson was instrumental in keeping me at Manchester as a Research Assistant.

My time in Hamburg was made memorable and highly enjoyable by Uda Albrecht, Molly Anderson, Phil and Monika Biddulph, Brian Cox, Big Chris, Little Chris, Beate Heinemann, Neil MacDonald, Dave Milstead, Julian Phillips, Eram Rizvi, Paul T, Asia T, William T, Hugh Tallini, Ben Waugh, Angela Wyatt and many others. Anna Burrage, Nick Malden and Rob Waugh made the Bleicherstraße days some of the best I can remember.

Keith Stephens sorted me out on the detector front, while Jim Weatherall was an inspiration both on and off the football field. Jim, Dave Futyan, Nick Savvas and all the HEP group at Manchester were great fun to be around.

Rosie Chitty, Gordon Cole, Natalie de Lima, Brandon Fernandez, Hilary Logan, Liz Potter, Mick Reynolds, Mark Roberts and Emma Shepley have all been wonderful, caring friends. Finally, I would like to thank my family for all their love, encouragement and support.

Only in Mathematics will you find Truth. (Cardinal Borusa)